

LA-UR-19-29164

Approved for public release; distribution is unlimited.

Title: A Correct Flat Field Model For DARHT

Author(s): Klasky, Marc Louis

Intended for: Report

Issued: 2019-09-12

Disclaimer:

Los Alamos National Laboratory, an affirmative action/equal opportunity employer, is operated by Triad National Security, LLC for the National Nuclear Security Administration of U.S. Department of Energy under contract 89233218CNA000001. By approving this article, the publisher recognizes that the U.S. Government retains nonexclusive, royalty-free license to publish or reproduce the published form of this contribution, or to allow others to do so, for U.S. Government purposes. Los Alamos National Laboratory requests that the publisher identify this article as work performed under the auspices of the U.S. Department of Energy. Los Alamos National Laboratory strongly supports academic freedom and a researcher's right to publish; as an institution, however, the Laboratory does not endorse the viewpoint of a publication or guarantee its technical correctness.

A Correct Flat Field Model For DARHT

Marc Klasky-P21

Los Alamos National Laboratory Report
August 21, 2019

Contents

1.0 Introduction	3
2.0 Forward Modeling	7
3.0 Flat-Field Simulations	11
4.0 Results.....	13
4.1 Magnitude and Characteristics of Scatter	13
4.1.1 FF Scatter with 5.2 cm of Tungsten in Bullnose.....	13
4.1.2 FF Scatter with 6.2 cm of Tungsten in Bullnose.....	20
4.1.3 FF Scatter with 7.2 cm of Tungsten in Bullnose.....	25
4.1.4 FF Scatter with 9.2 cm of Tungsten in Bullnose.....	31
4.1.5 FF Scatter with 11.2 cm of Tungsten in Bullnose.....	38
5 Comparison of Simulation Flat-Field with Scatter and Experimental Data	42
6 Proposed Forward Model/Ratio of Direct to Scatter and Functional fits.....	43
7.0 Conclusions	44
8.0 Acknowledgements	44
9.0 References	45

Figure 1 Forward Modeling Approach to Obtain Density of Unknown Objects.....	3
Figure 2 Radial Average of Beam Profile of DARHT Axis 2.....	4
Figure 3 DARHT Flat-Fields	5
Figure 4 DARHT Rough Collimator and Tungsten Plate Region.....	5
Figure 5 Beam Profile on Image Plane from Flat-Field	8
Figure 6 Direct Radiation on Image Plane given by Bremsstrahlung	9
Figure 7 Direct Transmission of Flat-Field Configurations.....	9
Figure 8 DARHT Radiographic Scene, Note: the FTO Collimator and FTO materials were voided out.....	11
Figure 9 DARHT Close-Up of DARHT Bull Nose Region, Tungsten Plates for Flat-Field, 5 cm Thick Plates, Density of Materials are indicated	12
Figure 10 DARHT Radiographic Near Detector Region Materials	12
Figure 11 Scatter field from Radiographic Tally, 5.2 cm Tungsten in the Bullnose at the Image Plane	14
Figure 12 Line-Outs of FF Scatter only using 5.2 cm Tungsten using Radiographic Tally at Image Plane	15
Figure 13 Total Signal 5.2 cm Tungsten in Bullnose using F4 Tally at Image Plane	15

Figure 14 Line-Outs of Total Signal from FF (Blue Row, Red Column) using 5.2 cm Tungsten in Bullnose performed using F4 Tally	16
Figure 15 Comparison of Total Flat-Field Signals with 5.2 cm Tungsten in Bullnose	16
Figure 16 Comparison of the Polynomial Fit (8X8) to the Total Signal (Scatter plus direct)	17
Figure 17 Ratio of Scatter to Direct 5.2 cm Tungsten	18
Figure 18 Row Averaged Line-out of Ratio of Scatter 5.2 cm Tungsten in Bullnose w/o NDM /w NDM	19
Figure 19 Ratio of Direct to Total 5.2 cm Tungsten in Bullnose	19
Figure 20 Scatter field from Radiographic Tally, 6.2 cm Tungsten in the Bullnose at the Image Plane	20
Figure 21 Line Outs Scatter (6.2 cm Tungsten in Bullnose) Radiographic Tally	21
Figure 22 Total (Direct and Scatter) (6.2 cm Tungsten in Bullnose) F4 Tally	21
Figure 23 Line-Outs of Total Signal from FF (Blue Row, Red Column) using 6.2 cm Tungsten in Bullnose performed using F4 Tally	22
Figure 24 Comparison of Total Flat-Field Signals with 6.2 cm Tungsten in Bullnose	22
Figure 25 Comparison of the Polynomial Fit (8X8) to the Total Signal (Scatter plus direct)	23
Figure 26 Ratio of Scatter to Direct 6.2 cm Tungsten	24
Figure 27 Ratio of Direct to Total 6.2 cm Tungsten in Bullnose	25
Figure 28 Scatter field from Radiographic Tally, 7.2 cm Tungsten in the Bullnose at the Image Plane	26
Figure 29 Line Outs Scatter (7.2 cm Tungsten in Bullnose) Radiographic Tally	26
Figure 30 Total (Direct and Scatter) (7.2 cm Tungsten in Bullnose) F4 Tally	27
Figure 31 Line-Outs of Total Signal from FF (Blue Column, Green Row) using 7.2 cm Tungsten in Bullnose performed using F4 Tally	27
Figure 32 Comparison of Total Flat-Field Signals with 7.2 cm Tungsten in Bullnose	28
Figure 33 Comparison of the Polynomial Fit (8X8) to the Total Signal (Scatter plus direct)	28
Figure 34 Ratio of Scatter to Direct 7 cm Tungsten	29
Figure 35 Ratio of Scatter 7.2 cm of Tungsten in Bullnose w/o NDM / w NDM	30
Figure 36 Ratio of Direct to Total 7.2 cm Tungsten in Bullnose	30
Figure 37 Scatter field from Radiographic Tally, 9.2 cm Tungsten in the Bullnose at the Image Plane	31
Figure 38 Line Outs Scatter (9.2 cm Tungsten in Bullnose) Radiographic Tally	32
Figure 39 Total (Direct and Scatter) (9.2 cm Tungsten in Bullnose) F4 Tally	32
Figure 40 Line-Outs of Total Signal from FF (Blue Column, Red Row) using 9.2 cm Tungsten in Bullnose performed using F4 Tally	33
Figure 41 Comparison of Total Flat-Field Signals with 9.2 cm Tungsten in Bullnose	34
Figure 42 Comparison of the Polynomial Fit (8X8) to the Total Signal (Scatter plus direct)	35
Figure 43 Ratio of Scatter to Direct 9.2 cm Tungsten	36

Figure 44 Ratio of Scatter 9.2 cm Tungsten in Bullnose w/o NDM / w NDM	37
Figure 45 Ratio of Direct to Total 9.2 cm Tungsten in Bullnose	38
Figure 46 Scatter field from Radiographic Tally, 11.2 cm Tungsten in the Bullnose at the Image Plane	39
Figure 47 Comparison of the Polynomial Fit (12X12) to the Total Signal (Scatter plus direct) 11 cm Tungsten in Bullnose	40
Figure 48 Ratio of Scatter to Direct 11 cm Tungsten	41
Figure 49 Ratio of Direct to Total 11.2 cm Tungsten in Bullnose	42
Figure 50 Comparison of the simulated flat-field 9.2 cm with the 3683 Axis 2 Time 1 Flat-Field 9.5 cm of Tungsten in the Bullnose	43

1.0 Introduction

The forward modeling approach has been utilized to obtain the density distribution during dynamic radiographic experiments using the Bayesian Inference Engine (BIE) at the Dual Axis Radiographic Hydrodynamic Test Facility (DARHT) for over two decades. The forward modeling approach attempts to incorporate all of the known physics to obtain the transmission, from an unknown density field. The density field is then optimized in an attempt to match the flat-fielded radiographic image using a Chi-squared comparison. A depiction of the forward modeling approach implemented in the BIE is given in Figure 1.ⁱⁱⁱ

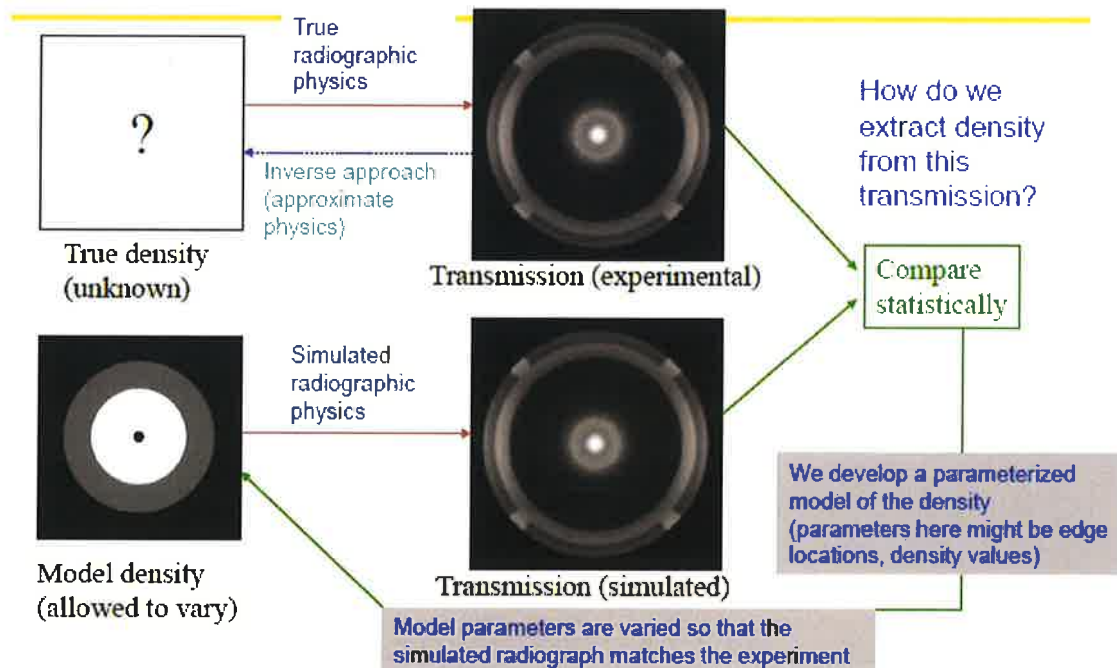


Figure 1 Forward Modeling Approach to Obtain Density of Unknown Objects

The experimental transmission of a dynamic image may be written as:

$$T_{EXP} = D_{EXP} + S_{EXP} \text{ Equation 1}$$

Where:

$T_{EXP} \equiv$ Experimental Dynamic Image

$D_{EXP} \equiv$ Experimental Direct Transmission

$S_{EXP} \equiv$ Experimental Scatter

The source utilized to generate the direct radiation on Axis 2 at DARHT is a nominal 16.8 Mev electron beam. The electron beam is magnetically focused onto a convertor target. The interaction of the electron beam with the convertor target produces a bremsstrahlung photon source. The photon source that is produced via the bremsstrahlung interaction generates a spatial profile on the image plane as may be observed from examination of Figure 2.

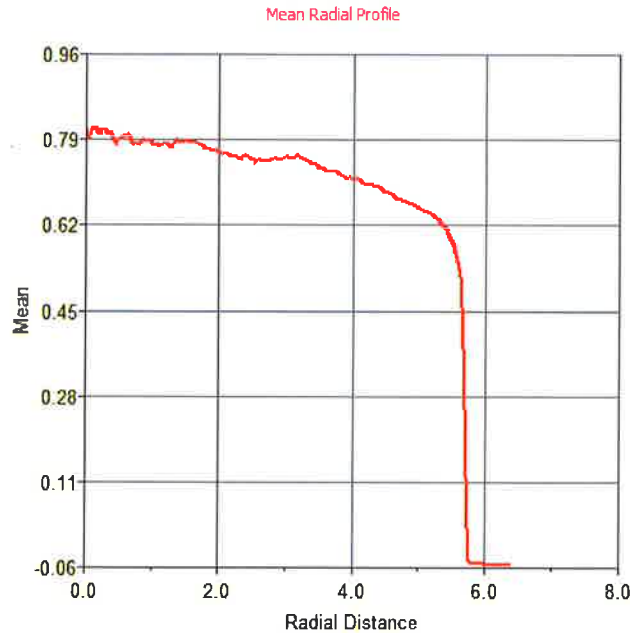


Figure 2 Radial Average of Beam Profile of DARHT Axis 2

As discussed below, DARHT images are flat-fielded to reduce the high frequency features of the scintillator as may be observed from examination of Figure 3.

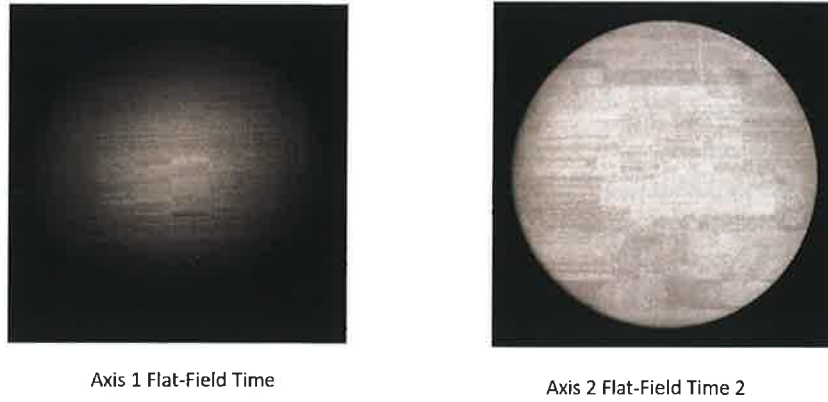


Figure 3 DARHT Flat-Fields

The flat-field image at DARHT is produced by placing Tungsten plates just in front of the rough collimator as illustrated in Figure 4. In these investigations a range of 5-11 cm of Tungsten has been examined.

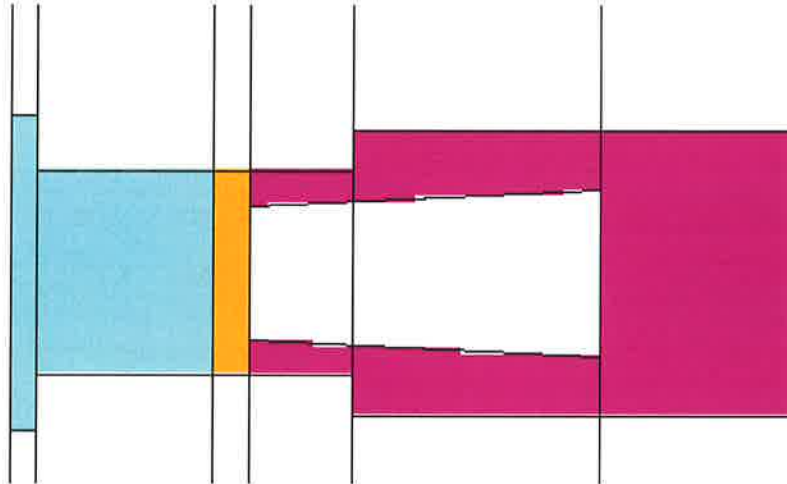


Figure 4 DARHT Rough Collimator and Tungsten Plate Region

The flat-fielded image acquired at DARHT may be written as:

$$T_{FF_EXP} = D_{FF_EXP} + S_{FF_EXP} \text{ Equation 2}$$

Where:

$T_{FF_EXP} \equiv$ Flat Field Experimental Image

$D_{FF_EXP} \equiv$ Flat Field Experimental Direct Transmission

$$S_{FF_EXP} \equiv \textit{Flat Field Experimental Scatter}$$

Consequently, the flat-fielded experimental dynamic image that the forward model attempts to match is given by:

$$\frac{T_{EXP}}{T_{FF_EXP}} = \frac{D_{EXP} + S_{EXP}}{D_{FF_EXP} + S_{FF_EXP}} \text{ Equation 3}$$

Having examined some general properties of the dynamic experimentally flat-fielded transmission reaching the image plane we now proceed to examine additional characteristics of the forward model.

2.0 Forward Modeling

The forward model implemented in the BIE produces a transmission of the dynamic experiment that may be written as:

$$\widetilde{T_{DFM}} = \widetilde{D_{DFM}} + \widetilde{S_{DFM}} \text{ Equation 4}$$

Where:

$$\check{T}_{DFM} = \text{Dynamic Forward Model Transmission}$$

$$\widetilde{D_{DFM}} \equiv \text{Direct component of the forward model transmission of the dynamic image}$$

$$\check{S}_{DFM} \equiv \text{Scatter component of the forward model transmission of the dynamic image}$$

In Equation 4 the direct radiation does not include the beam profile and may be written as:

$$\widetilde{D_{DFM}} = \int_{E_1}^{E_2} S(E) \exp^{-\sum_1^N \frac{\mu}{\rho}(E)_k \int \rho_k dl} dE \text{ Equation 5}$$

Where:

$$S(E) \equiv \text{Source Spectrum}$$

$$\frac{\mu}{\rho}(E) \equiv \text{Energy dependent cross sections}$$

$$\rho_k = \text{Path length of each material in the line of sight}$$

We may further develop the forward model for the transmission of a dynamic experiment by writing:

$$\check{T}_{DFM} = G(\check{D}_{DFM} B_{pD} + \check{S}_{DFM}) \text{ Equation 6}$$

Where:

$$B_{pD} \equiv \text{Beam profile produced during acquisition of the dynamic image}$$

$$G \equiv \text{System Gain} \times \text{Dose in the dynamic image}$$

To reduce the high frequency features of the scintillator DARHT images, as may be observed from examination of Figure 3, the images are flat-fielded. By placing tungsten plates of sufficient thickness to provide attenuation such that the camera gain is set to approximately match that utilized in the dynamic experiment the dynamic image is flat fielded. The use of Tungsten plates of sufficient thickness is provided to ensure linearity of the camera system between the dynamic image and the flat-fielded image.

The modulation of the direct radiation reaching the image plane from the flat-field may be modeled using MCNP6 by sending an electron into a converter target. In this calculation it is assumed that the electron beam is centered at the origin of the converter and is perpendicular to the converter target surface. (Deviations in the focusing of the electron beam will lead to different beam profiles and will be discussed below.) The resulting beam profile is given in Figure 5.

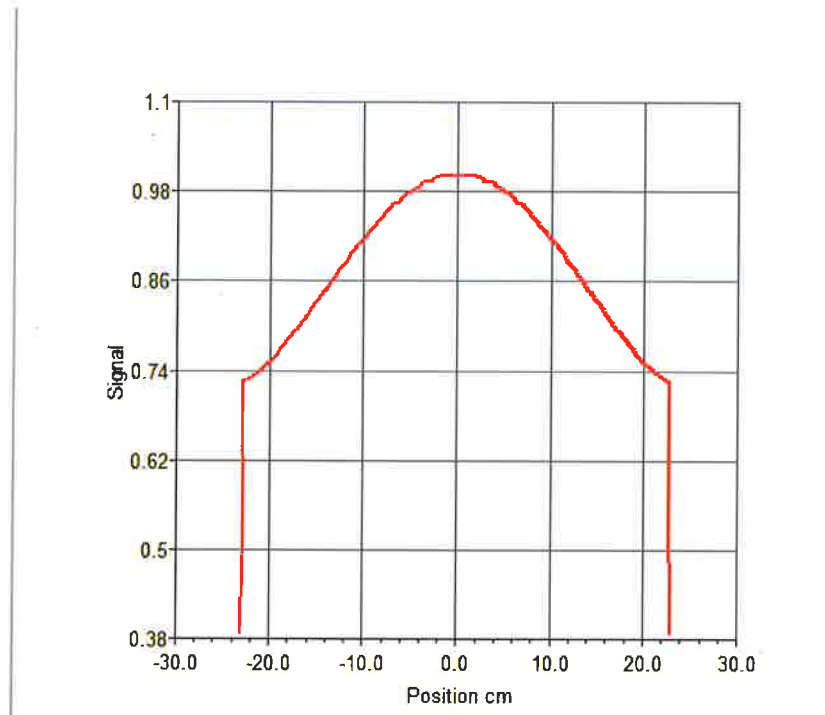


Figure 5 Beam Profile on Image Plane from Flat-Field

Examination of Figure 5 reveals a falloff of the direct transmission of approximately 27% from the axis to the edge of the field of view at DARHT. This falloff is a unique property of the bremsstrahlung radiation generated by the electron beam interacting with the converter target. Simulations demonstrating the spatial fall-off of the beam profile reaching the image plane in the Flat-Field geometry at DARHT were obtained by running MCNP6 simulations incorporating both the energy spectra and the angular distribution of the photons by colliding a 16.8 Mev electron onto a 1 mm converter target. All direct simulations were obtained by using the radiographic tally NOTRN option with the coherent scatter cross section included in the total attenuation. Normalized profiles for the range of Tungsten plates examined are presented in Figure 6.

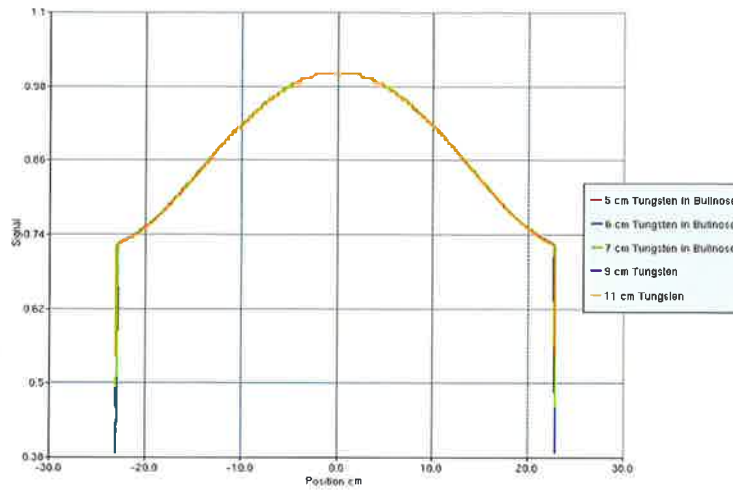


Figure 6 Direct Radiation on Image Plane given by Bremsstrahlung

The total attenuation of the un-collided beam reaching the image plane is illustrated in Figure 7.

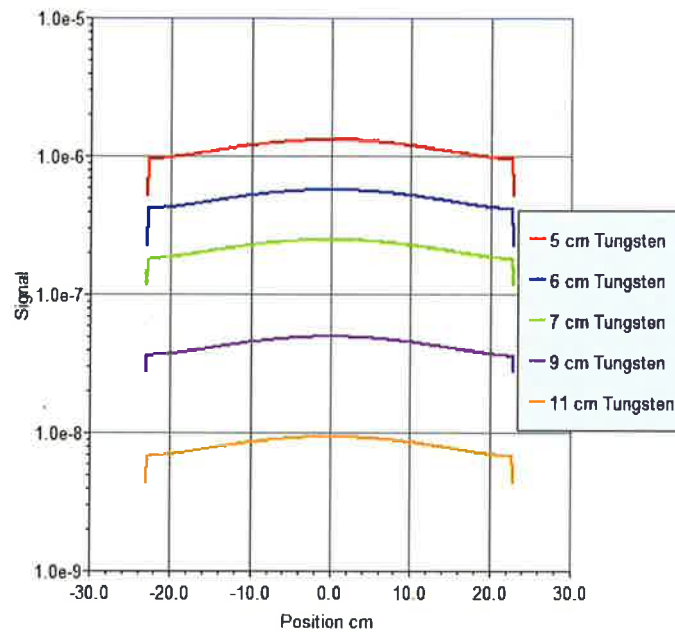


Figure 7 Direct Transmission of Flat-Field Configurations

Using this knowledge we now write an expression for the flat-field forward model.

The transmission of the flat field may be written as:

$$\check{T}_{FF} = G^1(\check{D}_{FF} \check{B}_{pFF} + \check{S}_{FF}) \text{ Equation 7}$$

Where:

$$\begin{aligned} G^1 &\equiv \text{Gain of system } \times \text{ Dose} \\ \check{D}_{FF} &\equiv \text{Direct image of the Flat Field} \\ \check{B}_{pFF} &\equiv \text{Beam profile obtained during the flat field} \\ \check{S}_{FF} &\equiv \text{Scatter in the Flat Field} \end{aligned}$$

The ratio of the dynamic image to the flat-fielded image may be written as:

$$G'' \left(\frac{\check{D}_{DFM} \check{B}_{pD} + \check{S}_{DFM}}{\check{D}_{FF} \check{B}_{pFF} + \check{S}_{FF}} \right) \text{ Equation 8}$$

Where:

$$G'' = \frac{G}{G^1} = \text{scalar multiple}$$

If we assume that the scatter in the flat-field is negligible and define the ratio of the beam profiles during the dynamic experiment and the flat-field as:

$$B \equiv \frac{\check{B}_{pD}}{\check{B}_{pF}}$$

Noting that \check{D}_{FF} is unity we may write:

$$G'' \left(\check{D}_{DFM} B + \frac{\check{S}_{DFM}}{\check{B}_{pFF}} \right) \text{ Equation 9}$$

Before proceeding we note that the ratio of the flat-fields of the dynamic image and the flat-field may have a complicated structure and thereby require many degrees of freedom to correctly capture. We suggest that this aspect of the problem due to the variability of the electron focusing on the convertor target be modeled by allowing the two flat-fields to shift and rotate relative to one another. However, further investigation of this is needed.

It should be noted that during the dynamic the position of the spot is not precisely known and consequently the resulting beam profile has been obtained via an empirical fit. Given the necessity to introduce unknowns into the highly non-linear, non-convex forward model functional, this may have an impact on the ability to correctly estimate the density optimized to obtain a match to the experimentally flat-fielded transmission.

In the remainder of this report we examine the previous assumption that the scatter in the flat-field is negligible compared to the direct signal.^{iv} Following this investigation, a new formulation of the forward model incorporating both the beam profile as well as the scatter in the flat-field is presented. The results of these investigations are then fitted with smooth functions to allow these results to be easily incorporated into a glyph that is proposed to be included into future BIE forward models.

3.0 Flat-Field Simulations

In this section we describe the setup of the MCNP simulations to examine the nature of the scatter produced in the Flat-Field images.

MCNP transport simulations were performed using the radiographic scene as depicted in Figure 8-Figure 10.

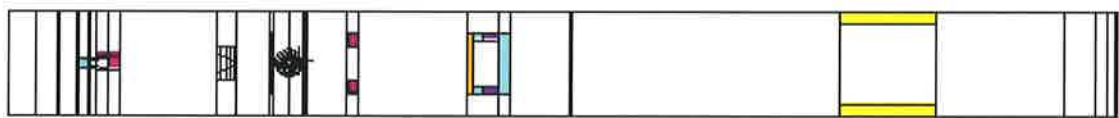


Figure 8 DARHT Radiographic Scene, Note: the FTO Collimator and FTO materials were voided out

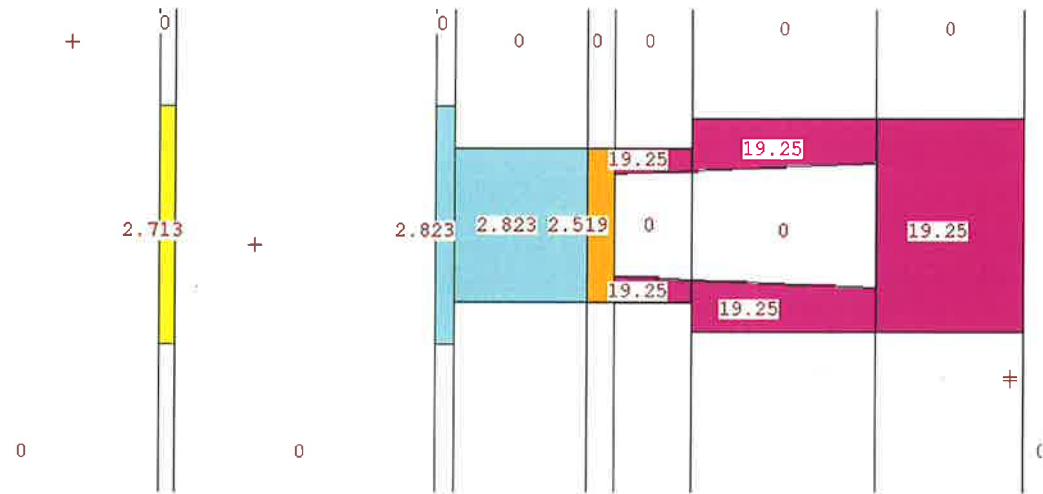


Figure 9 DARHT Close-Up of DARHT Bull Nose Region, Tungsten Plates for Flat-Field, 5 cm Thick Plates, Density of Materials are indicated

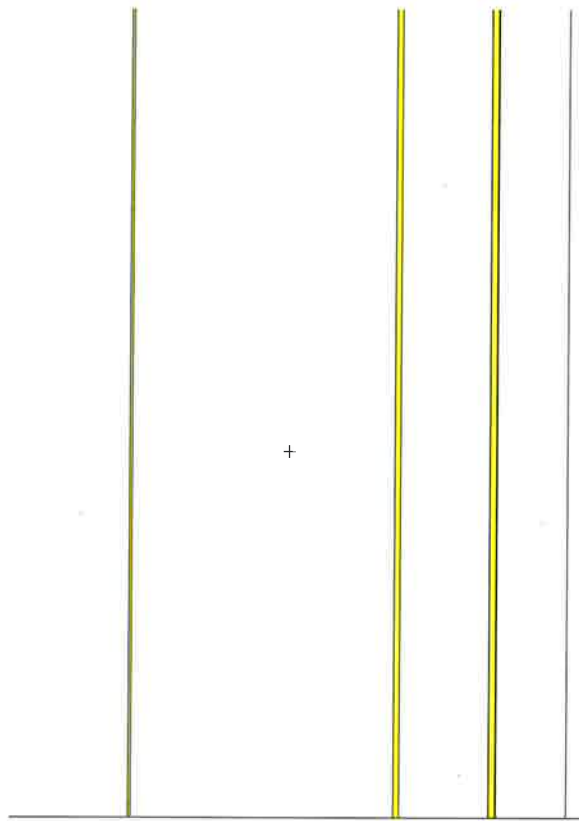


Figure 10 DARHT Radiographic Near Detector Region Materials

Before proceeding it should be noted that the density of the Tungsten in the Bullnose calculations erroneously utilized 19.25 g/cm^3 in lieu of the actual number of 18.5 g/cm^3 . The effect of this density difference is to simply modify the thickness of the Tungsten plates. Consequently, in the remainder of this report we modify the Tungsten thicknesses by the ratio $19.25/18.5$. Thus, a thickness of 5 cm in the calculation corresponds to 5.2 cm.

A range of Tungsten plates placed in the bull-nose were examined as part of this investigation. The simulations were run with full electron physics as well as with coherent scatter using both the radiographic tally as well as with an F4 tally. It should be noted that in the configurations studied the Near Detector Materials as given in Figure 10 were incorporated into all simulations. (Investigations of the scatter without the NDM were also performed and will be reported in this publication.) It also may be noted that previous studies have demonstrated that incorporation of these materials into the forward model are essential in reproducing the scatter in the forward model. ^v That is, the proximity of these materials to the image plane creates a correlated scatter component that **cannot be adequately fitted without an explicit model**. (Failure to incorporate this correlated scatter into the scatter field will result in density errors in the reconstruction.) This

Physics has only recently been incorporated into the forward model.^{vi} Before presenting the results of the Flat-Field investigation it must be emphasized that a proper scatter model must also be implemented into the forward model in conjunction with the Flat Field forward model presented in this work to obtain an accurate density reconstruction. Failure to implement a proper physics based scatter model which has been shown to exclude the previous so called “principled approach” will result in unacceptable density reconstructions, i.e., the density errors will be larger than those incorporating a physics model when the Bucky Grid is not present.^{vii} (These statement only apply to DARHT Axis II.) The basis for this statement is that scatter has been demonstrated to have significant curvature that is attributed to both coherent scatter as well as the Near Detector Materials in close proximity to the image plane. Furthermore, the lack of separability of the scatter from the direct transmission in the forward model will lead to density errors if higher order polynomials are utilized to attempt to obtain the scatter field over the entire domain of the image. Therefore, previous models which utilize empirical models for the scatter on DARHT Axis II will lead to larger density errors than physics based model and consequently will not properly characterize the density errors at DARHT but rather are probably much more attributed to epistemic errors.

4.0 Results

In this Section we present the results of the MCNP6 transport simulations to evaluate the scattered radiation arising from the flat-field images. To obtain the characteristics of scatter from the Flat-Field scenes a range of Tungsten thicknesses in the bullnose (5-11 cm) were examined using MCNP6. These simulations incorporated all materials in the Line-of-Sight as well as the materials from the enclosure of the gamma ray camera as illustrated in Figure 10. All calculations were performed using full electron physics as well as coherent scatter. In addition, the calculations included both the bremsstrahlung photon energy spectra as well as the angular dependence of the bremsstrahlung source. The calculations were performed using both the radiographic tally as well as the F4 results to confirm the results. In addition, to quantify the amount of scatter from the NDM, calculations were also performed without these materials.

4.1 Magnitude and Characteristics of Scatter

4.1.1 FF Scatter with 5.2 cm of Tungsten in Bullnose

The results of the scatter field using the radiographic tally in which 5 cm of Tungsten was incorporated into the bullnose are presented in Figure 11.

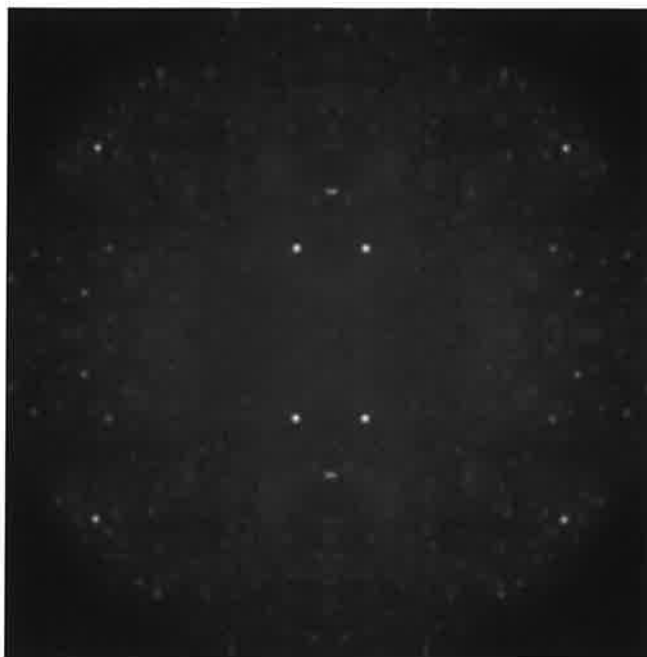


Figure 11 Scatter field from Radiographic Tally, 5.2 cm Tungsten in the Bullnose at the Image Plane

As may be observed, the results using the radiographic tally have a significant number of flyers due to the proximity of the NDM to the image plane. (It should be noted that the pre-collision next event estimator implemented via the PDS card to minimize the impact of flyers from both the coherent scattering as well as scatters in proximity to the radiographic image plane was utilized in all calculations in which the radiographic tally was applied. While this variance reduction technique reduced the flyers from the coherent scatters it did not do so for the NDM.) Line-outs of the scatter using both rows and columns are presented in Figure 12.

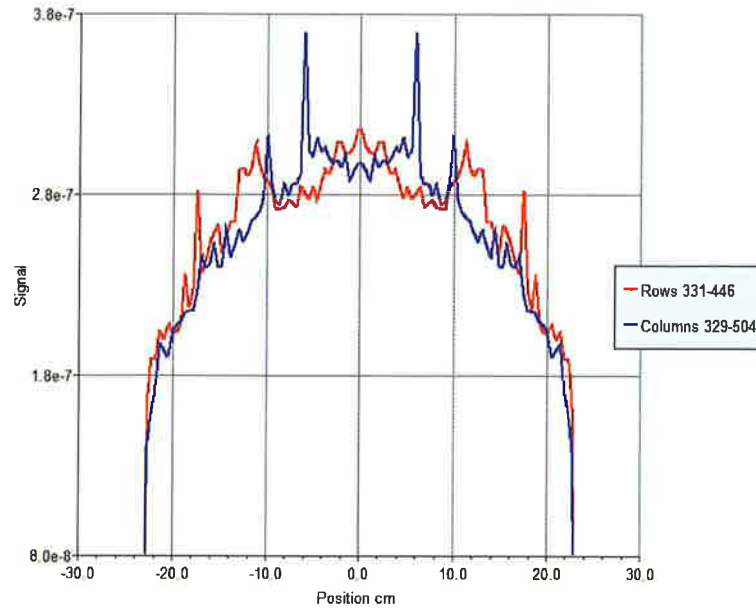


Figure 12 Line-Outs of FF Scatter only using 5.2 cm Tungsten using Radiographic Tally at Image Plane

A simulation of the total signal (scatter and direct) using the F4 tally was also performed. The total signal, i.e., scatter and direct is presented in Figure 13.



Figure 13 Total Signal 5.2 cm Tungsten in Bullnose using F4 Tally at Image Plane

It should be noted that the calculation was run with 8.5×10^{10} particles and had in general very good statistical error properties passing all statistical convergence tests.

Line-outs of the scatter using both rows and columns for the 5 cm of Tungsten case in the bullnose performed with the F4 tally are presented in Figure 14.

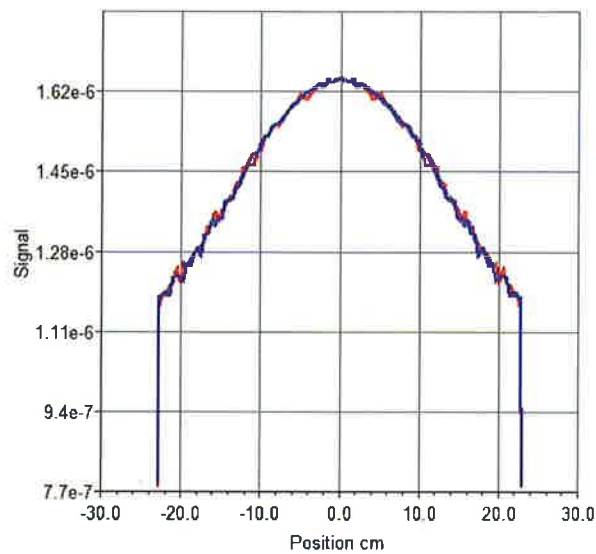


Figure 14 Line-Outs of Total Signal from FF (Blue Row, Red Column) using 5.2 cm Tungsten in Bullnose performed using F4 Tally

A comparison of the total signal using both the radiographic tally and the F4 tally is presented in Figure 15.

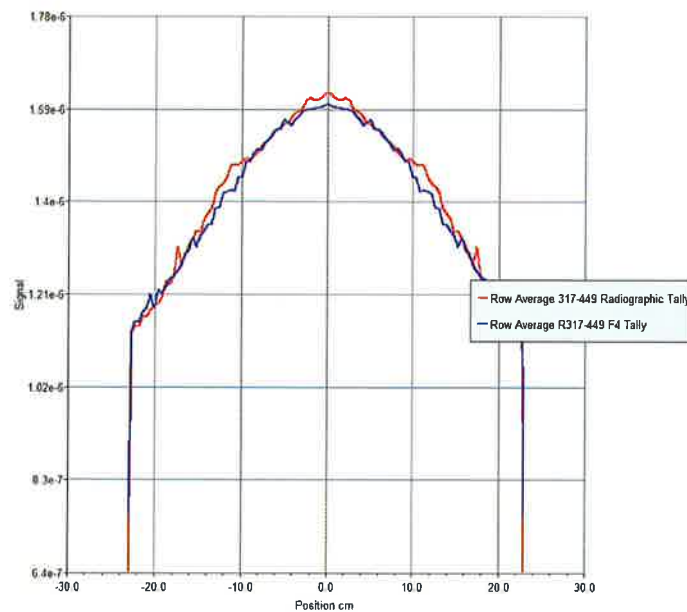


Figure 15 Comparison of Total Flat-Field Signals with 5.2 cm Tungsten in Bullnose

Examination of Figure 15 shows good agreement between the two calculations. However, while the radiographic tally suffers from the presence of flyers, the F4 simulation suffers from high frequency noise. Consequently, we chose to utilize the radiographic tally to capture the total

flat-field signal, i.e., direct plus scatter. To perform this fit we utilized an 8x8 order polynomial field. A comparison of the polynomial fit and the MCNP simulation using the radiographic tally for the total signal arising from 5.2 cm of Tungsten in the bullnose in conjunction with the DARHT radiographic scene is presented in Figure 16.

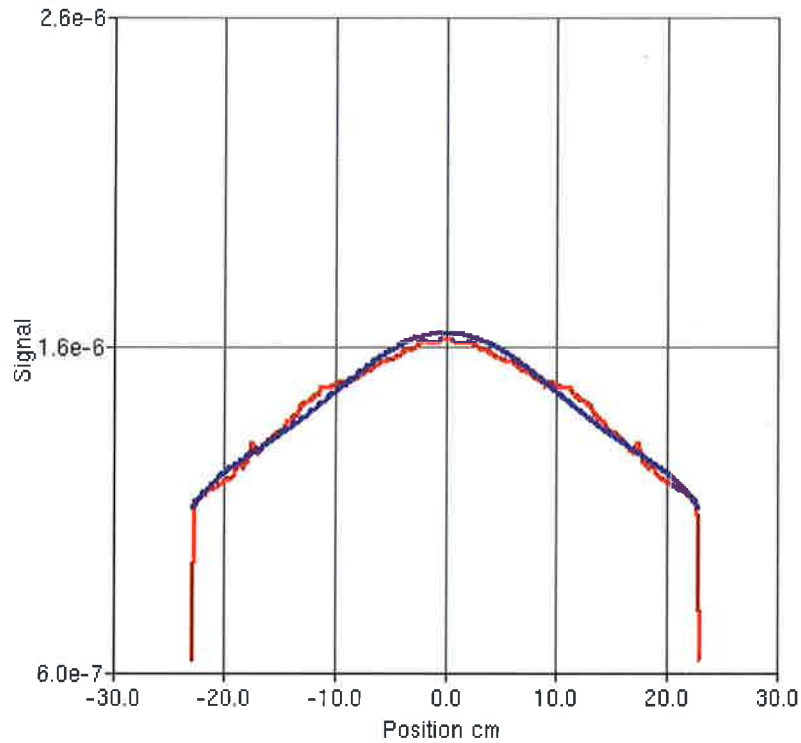


Figure 16 Comparison of the Polynomial Fit (8X8) to the Total Signal (Scatter plus direct)

Examination of Figure 16 illustrates the fact that the 8x8 polynomial fit provides an excellent fit to the simulation.

Similarly using a functional (8X8 polynomial) a fit to the scatter obtained from the radiographic tally was obtained and compared to the direct signal as illustrated in Figure 17.

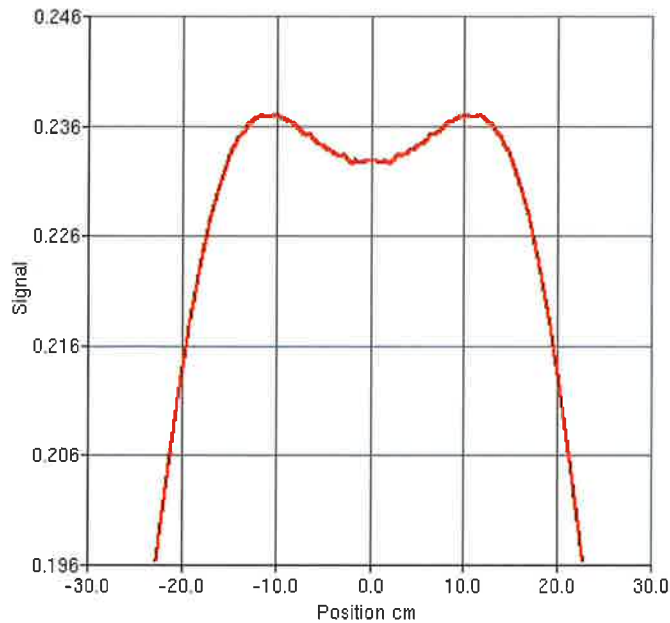


Figure 17 Ratio of Scatter to Direct 5.2 cm Tungsten

Examination of Figure 17 clearly demonstrates that even with a small amount of material in the bullnose the scatter is a significant fraction of the direct signal. It should also be noted that while the ratio of the scatter to direct is approximately constant over most of the image there is a substantial variation in the ratio outside of approximately 15 cm, at the image plane, or approximately 4 cm at the object. A falloff in the ratio of the scatter to direct is then observed in the scatter as one approaches the edge of the field of view. This magnitude of scatter is in part attributed to the presence of the NDM as illustrated in Figure 18.

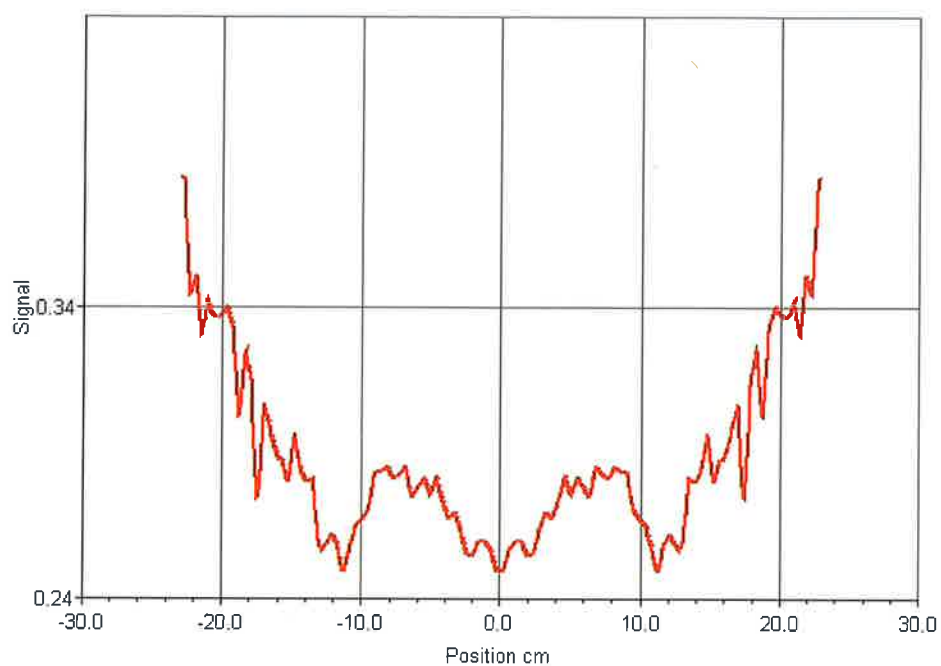


Figure 18 Row Averaged Line-out of Ratio of Scatter 5.2 cm Tungsten in Bullnose w/o NDM /w NDM

Finally, the ratio of the direct to the total signal (direct plus scatter) is presented in Figure 19.

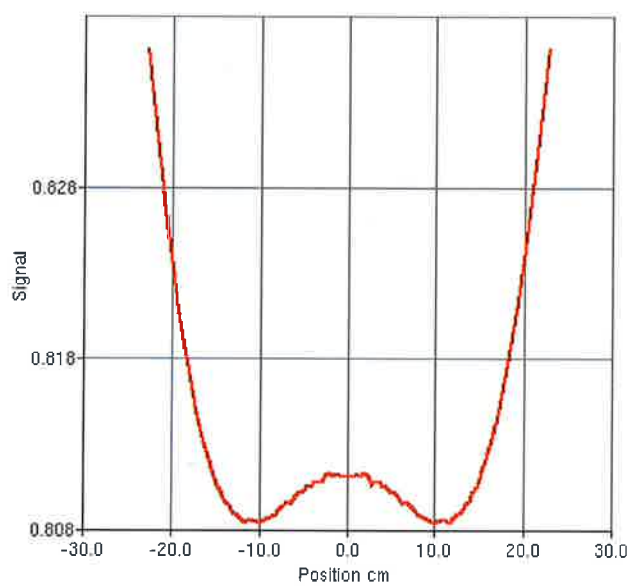


Figure 19 Ratio of Direct to Total 5.2 cm Tungsten in Bullnose

As may be observed from examination of Figure 19 there are variations at the few percent level in transmission.

4.1.2 FF Scatter with 6.2 cm of Tungsten in Bullnose

The results of the scatter field using the radiographic tally in which 6 cm of Tungsten was incorporated into the bullnose are presented in Figure 20.

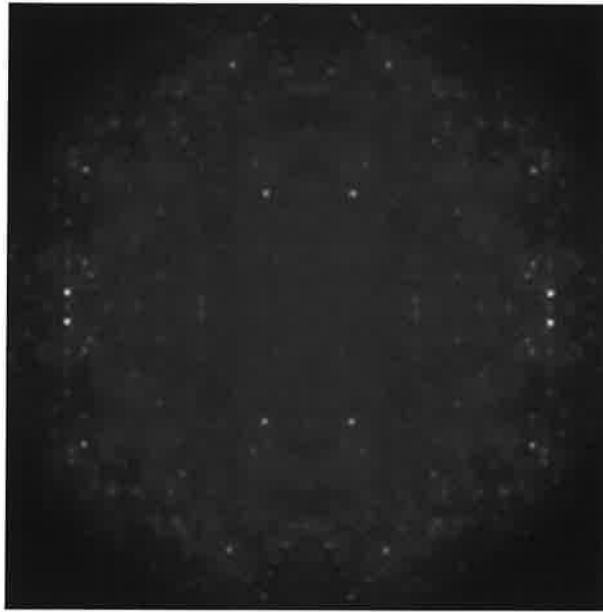


Figure 20 Scatter field from Radiographic Tally, 6.2 cm Tungsten in the Bullnose at the Image Plane

As may be observed, the results using the radiographic tally again have a significant number of flyers due to the proximity of the NDM to the image plane albeit somewhat lower than the 5.2 cm of Tungsten. Line-outs of the scatter using both rows and columns are presented in Figure 21.

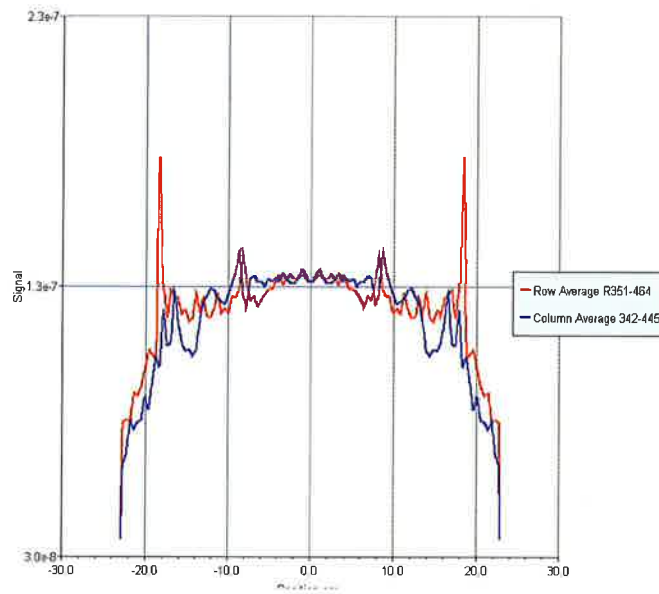


Figure 21 Line Outs Scatter (6.2 cm Tungsten in Bullnose) Radiographic Tally

A simulation of the total signal (scatter and direct) using the F4 tally was also performed. The total signal i.e. scatter and direct is presented in Figure 22.

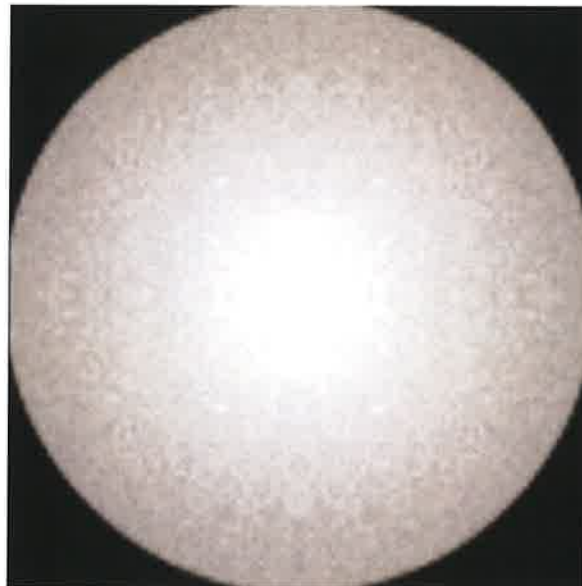


Figure 22 Total (Direct and Scatter) (6.2 cm Tungsten in Bullnose) F4 Tally

Line-outs of the scatter using both rows and columns for the 6.2 cm of Tungsten case in the bullnose performed with the F4 tally are presented in Figure 23.

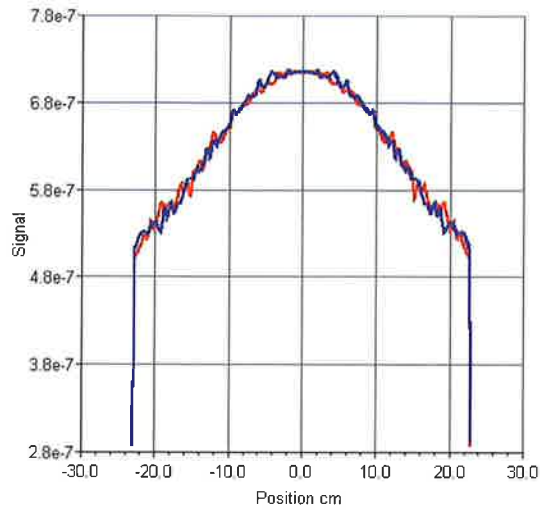


Figure 23 Line-Outs of Total Signal from FF (Blue Row, Red Column) using 6.2 cm Tungsten in Bullnose performed using F4 Tally

A comparison of the total signal using both the radiographic tally and the F4 tally is presented in Figure 24.

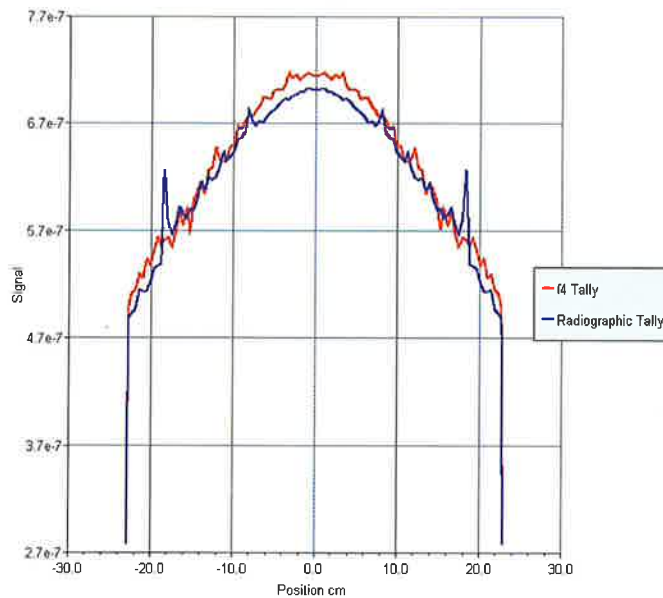


Figure 24 Comparison of Total Flat-Field Signals with 6.2 cm Tungsten in Bullnose

Examination of Figure 24 shows reasonably good agreement between the two calculations. However, while the radiographic tally suffers from the presence of flyers, the F4 suffers from high frequency noise. Consequently, we chose to fit the radiographic tally to capture the total

flat-field signal, i.e., direct plus scatter. To perform this fit we again utilized an 8x8 order polynomial field. A comparison of the polynomial fit and the MCNP simulation using the radiographic tally for the total signal arising from the 6.2 cm of Tungsten in the bullnose in conjunction with the DARHT radiographic scene is presented in Figure 25.

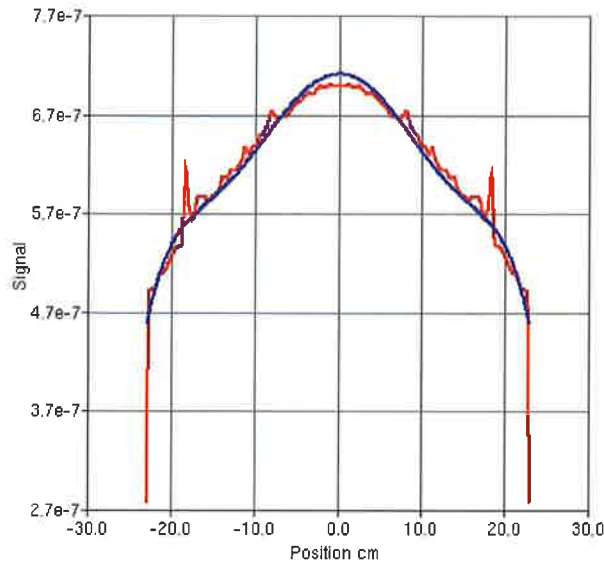


Figure 25 Comparison of the Polynomial Fit (8X8) to the Total Signal (Scatter plus direct)

Examination of Figure 25 illustrates the fact that the 8x8 polynomial fit allows for an excellent comparison with the simulation.

Similarly, using the functional fit to scatter (8X8 polynomial) obtained using the radiographic tally the ratio of scatter to the direct is presented in Figure 26.

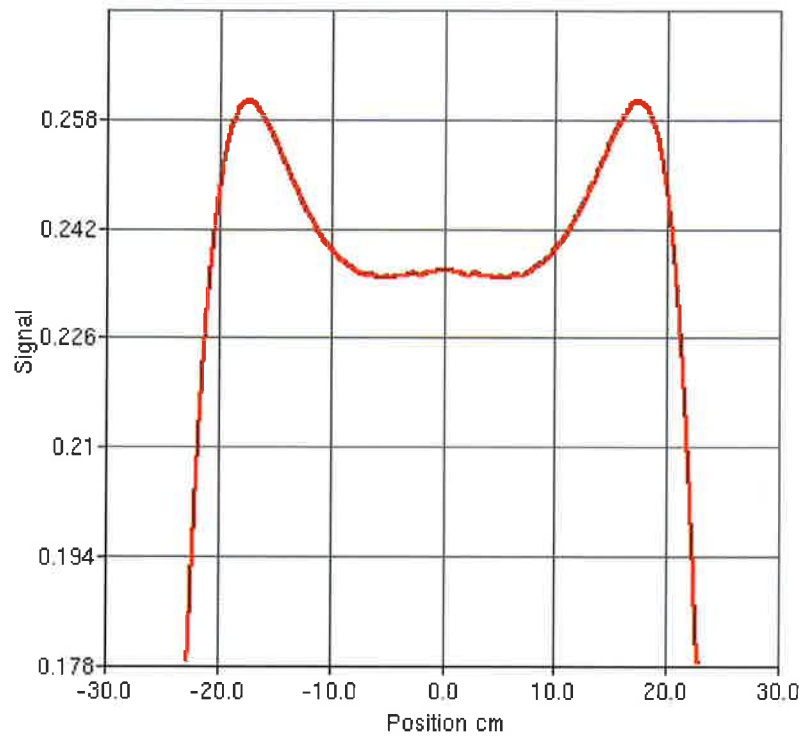


Figure 26 Ratio of Scatter to Direct 6.2 cm Tungsten

Examination of Figure 26 again clearly demonstrates that even flat-fields incorporating a relatively small amount of material in the bullnose lead to a significant fraction of scatter relative to the direct signal.

Further examination of Figure 26 again reveals a region across the image of relatively constant scatter followed by behavior as observed previously.

Finally, the ratio of the direct to the total signal (direct plus scatter) is presented in Figure 27.

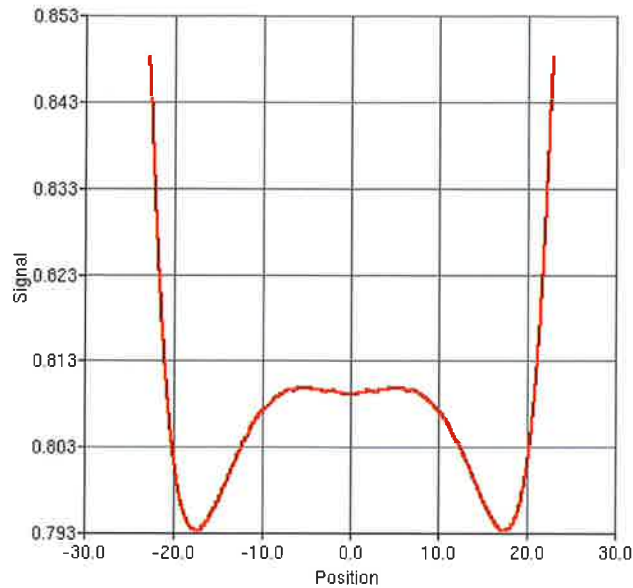


Figure 27 Ratio of Direct to Total 6.2 cm Tungsten in Bullnose

Examination of Figure 27 reveals relatively large deviations in the direct to total signal in the fiducial region. This behavior provides another rationale for why the models in which the flat-field was previously not explicitly modeled and where the “principled” approach to capture scatter in the fiducial region **could not work well**. (The other reason being the physical nature of the scatter attributed to both coherent scatter as well as scatter attributed to the NDM.) It should also be noted that this is not to suggest that simple inclusion of the flat-field model will enable the “principled approach” to work. That is, as previously demonstrated the physics of scatter is such that the coherent scatter as well as the NDM lead to curvature such that the scatter cannot be adequately obtained in the fiducial region. Therefore, a new physics based model as has been previously suggested and utilized on Hydro-tests must be utilized in conjunction with the model for the flat-field.^{viii,ix}

4.1.3 FF Scatter with 7.2 cm of Tungsten in Bullnose

The results of the scatter field using the radiographic tally in which 7.2 cm of Tungsten was incorporated into the bullnose are presented Figure 28.

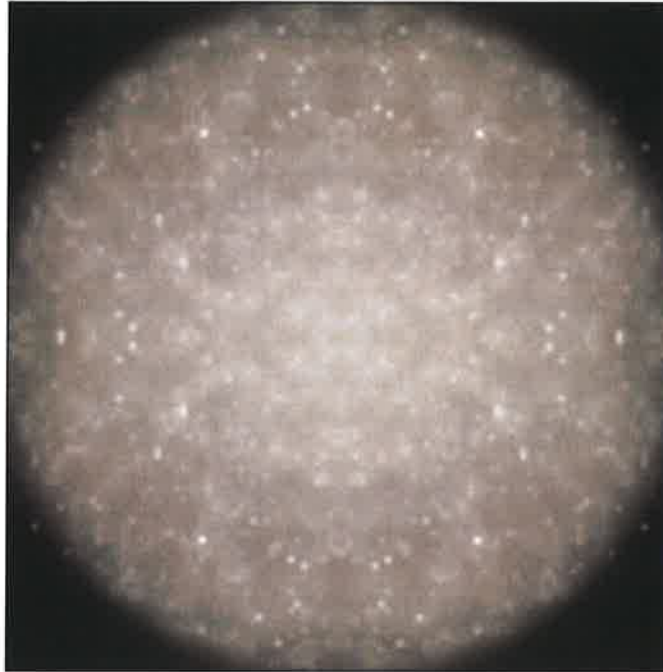


Figure 28 Scatter field from Radiographic Tally, 7.2 cm Tungsten in the Bullnose at the Image Plane

As may be observed, the results using the radiographic tally again have a significant number of flyers due to the proximity of the NDM to the image plane. Line-outs of the scatter using both rows and columns are presented in Figure 29.

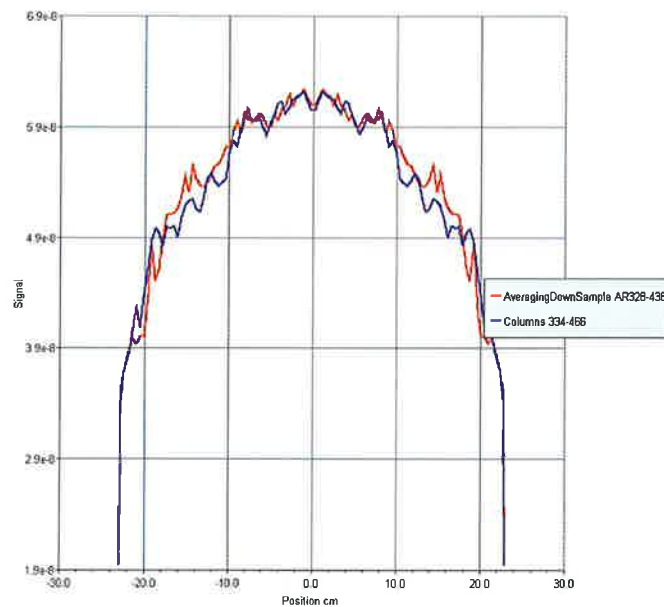


Figure 29 Line Outs Scatter (7.2 cm Tungsten in Bullnose) Radiographic Tally

A simulation of the total signal (scatter and direct) using the F4 tally was also performed. The total signal, i.e., scatter and direct is presented in Figure 30.

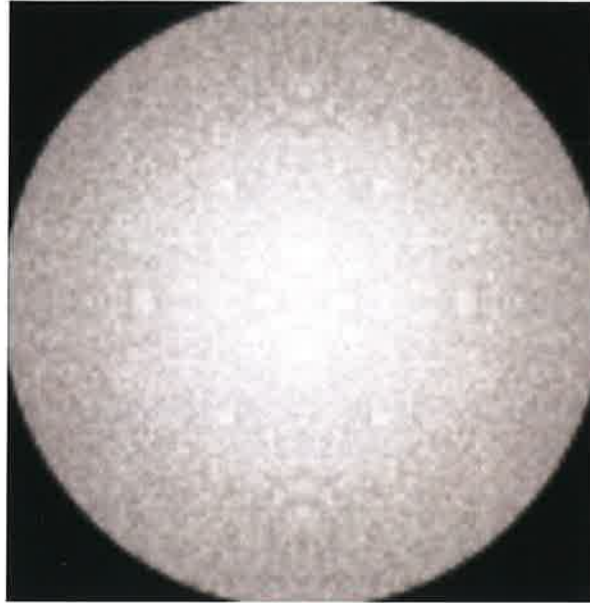


Figure 30 Total (Direct and Scatter) (7.2 cm Tungsten in Bullnose) F4 Tally

Line-outs of the scatter using both rows and columns for the 7.2 cm of Tungsten case in the bullnose performed with the F4 tally are presented in Figure 31.

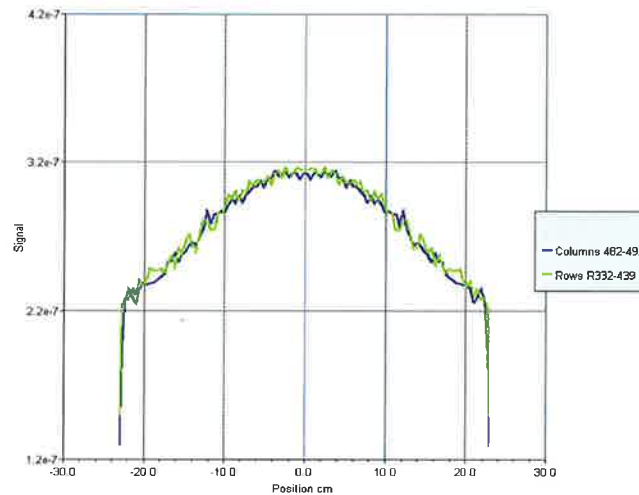


Figure 31 Line-Outs of Total Signal from FF (Blue Column, Green Row) using 7.2 cm Tungsten in Bullnose performed using F4 Tally

A comparison of the total signal using both the radiographic tally and the F4 tally are presented in Figure 32.

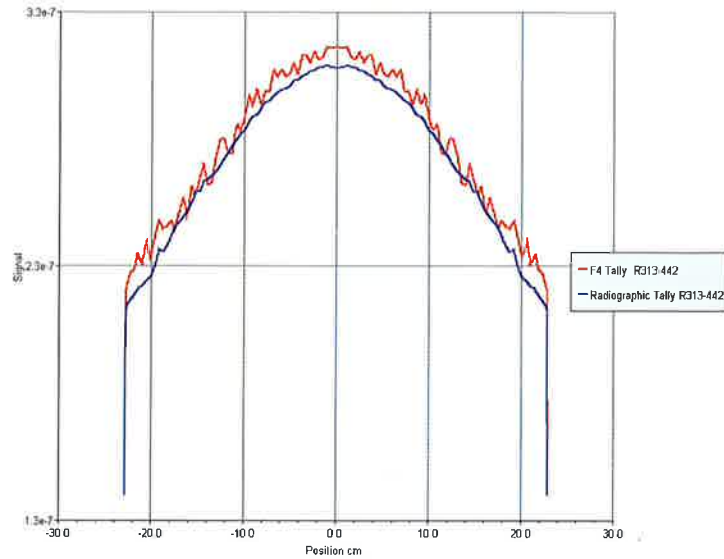


Figure 32 Comparison of Total Flat-Field Signals with 7.2 cm Tungsten in Bullnose

Examination of Figure 32 shows reasonable agreement between the two calculations. However, while the radiographic tally suffers from the presence of flyers, the F4 suffers from high frequency noise. Consequently, we chose to fit the scatter using the radiographic tally to capture the total flat-field signal, i.e., direct plus scatter. To perform this fit we utilized an 8x8 order polynomial field. A comparison of the polynomial fit and the MCNP simulation using the radiographic tally for the total signal arising from the 7.2 cm of Tungsten in the bullnose in conjunction with the DARHT radiographic scene is presented in Figure 29.

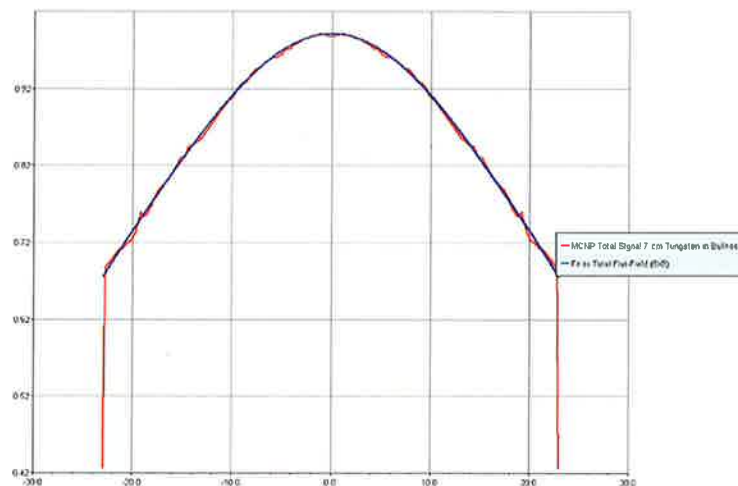


Figure 33 Comparison of the Polynomial Fit (8X8) to the Total Signal (Scatter plus direct)

Examination of Figure 33 illustrates the fact that the 8x8 polynomial fit allows for an excellent fit with the simulation.

Similarly, the scatter from the radiographic tally simulation may be fit using a functional fit (8X8 polynomial) to obtain the ratio of scatter to the direct, Figure 34.

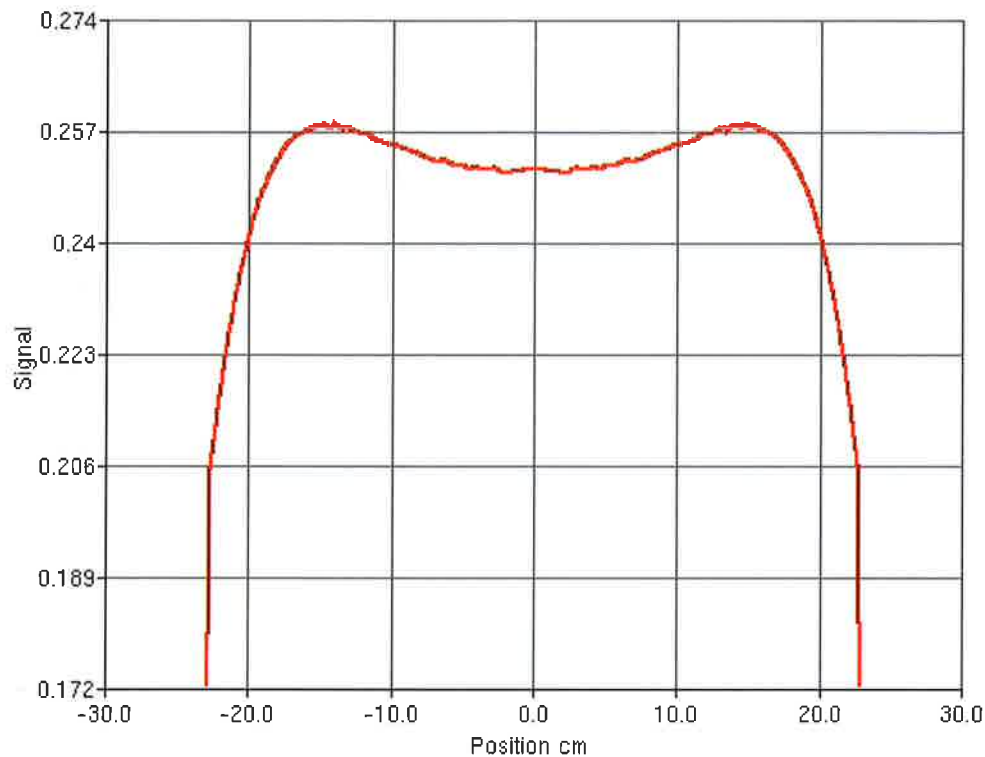


Figure 34 Ratio of Scatter to Direct 7 cm Tungsten

Examination of Figure 34 clearly demonstrates that scatter is a significant fraction of the direct signal. We again observe a similar modulation in the ratio of the scatter to direct signal in proximity to the edge as observed with the 5 cm and 6 cm Tungsten cases. Further examination of Figure 34 again reveals a region across the image of relatively constant scatter followed by behavior.

This magnitude of scatter is in part attributed to the presence of the NDM as illustrated in Figure 35.

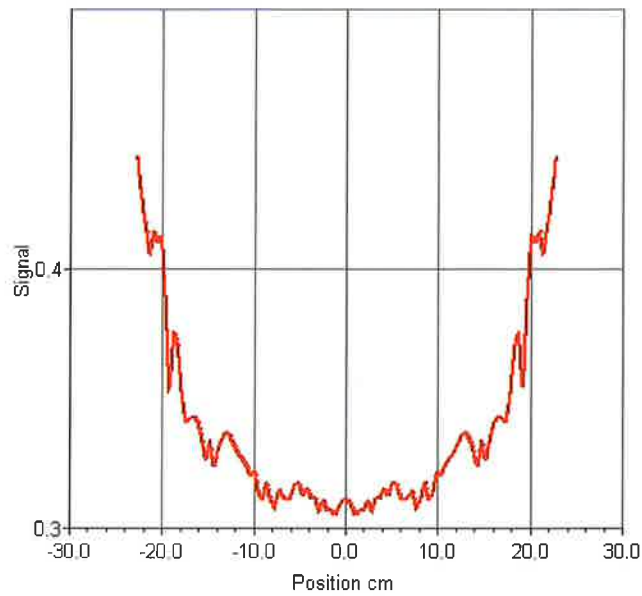


Figure 35 Ratio of Scatter 7.2 cm of Tungsten in Bullnose w/o NDM / w NDM

Finally, the ratio of the direct to the total signal (direct plus scatter) is presented in Figure 36.

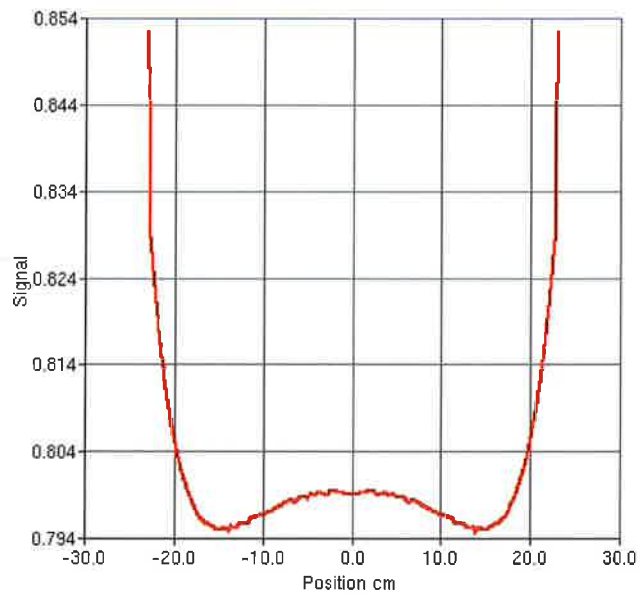


Figure 36 Ratio of Direct to Total 7.2 cm Tungsten in Bullnose

Examination of Figure 36 again reveals relatively large deviations in the direct to total signal in proximity to the image edge.

4.1.4 FF Scatter with 9.2 cm of Tungsten in Bullnose

The results of the scatter field using the radiographic tally in which 9.2 cm of Tungsten was incorporated into the bullnose are presented in Figure 37.

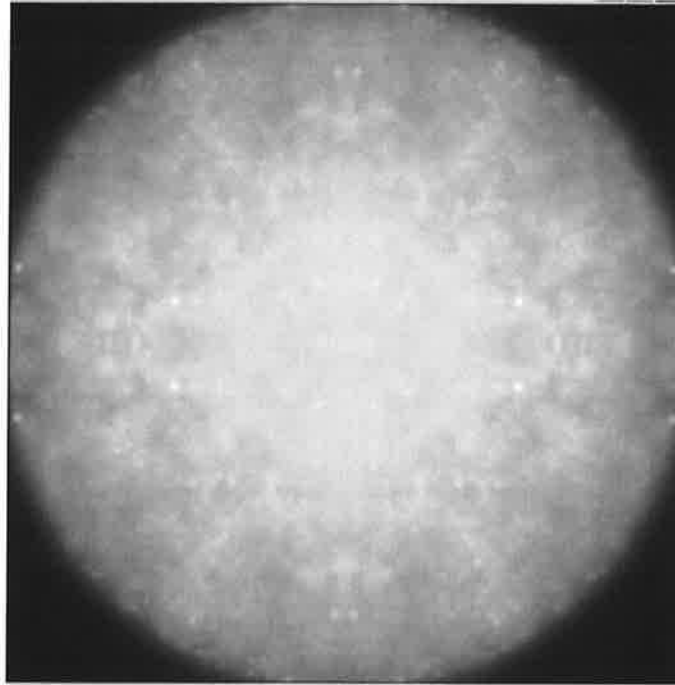


Figure 37 Scatter field from Radiographic Tally, 9.2 cm Tungsten in the Bullnose at the Image Plane

As may be observed, the results using the radiographic tally again have a significant number of flyers due to the proximity of the NDM to the image plane. Line-outs of the scatter using both rows and columns are presented in Figure 38.

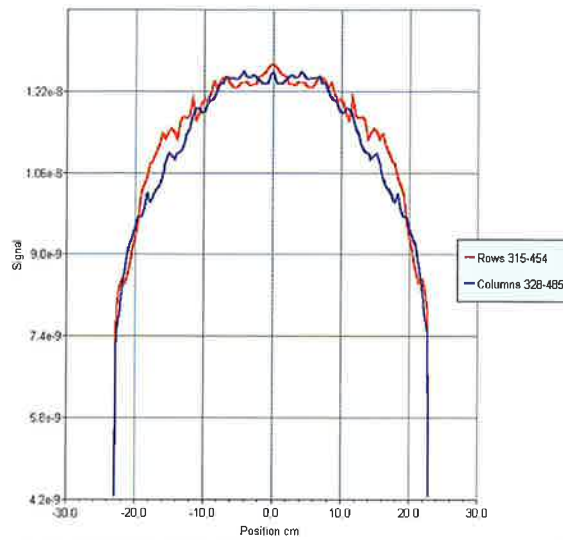


Figure 38 Line Outs Scatter (9.2 cm Tungsten in Bullnose) Radiographic Tally

A simulation of the total signal (scatter and direct) using the F4 tally was also performed. The total signal, i.e., scatter and direct is presented in Figure 39.

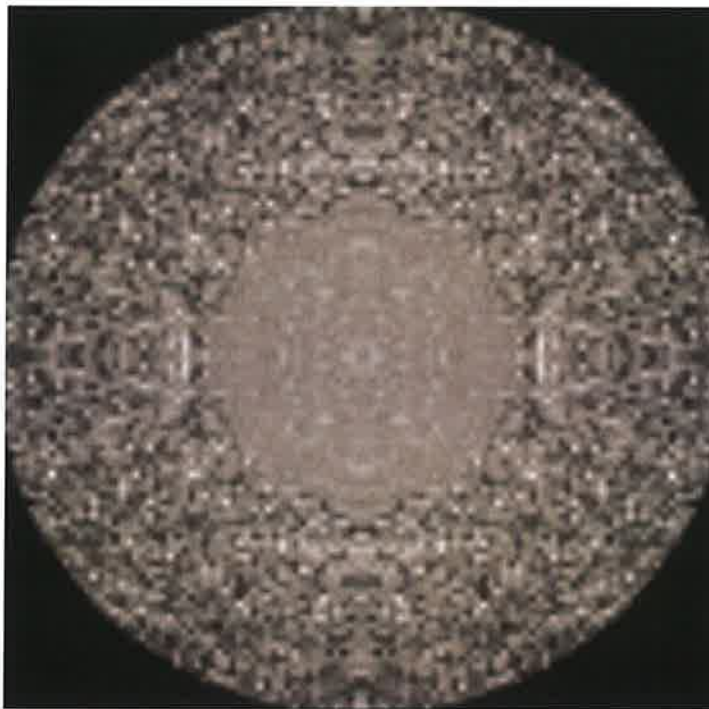


Figure 39 Total (Direct and Scatter) (9.2 cm Tungsten in Bullnose) F4 Tally

Examination of Figure 39 reveals unacceptable convergence in the results despite running

7.7×10^{10} particles. Most of the relative errors are in excess of 0.1. These results would require at least double the number of particles to have reasonable convergence properties. Consequently, for attenuations in this **regime it is recommended that the radiographic tally be utilized** to avoid excessive computational time. Nevertheless, we present line-outs of the scatter using both rows and columns for the 9.2 cm of Tungsten case in the bullnose performed with the F4 tally in Figure 40.

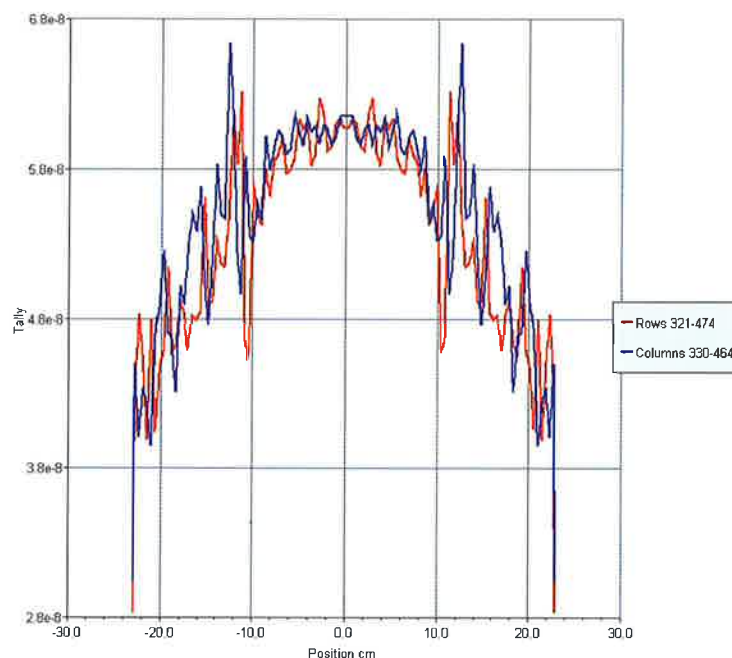


Figure 40 Line-Outs of Total Signal from FF (Blue Column, Red Row) using 9.2 cm Tungsten in Bullnose performed using F4 Tally

A comparison of the total signal using both the radiographic tally and the F4 tally is presented in Figure 41.

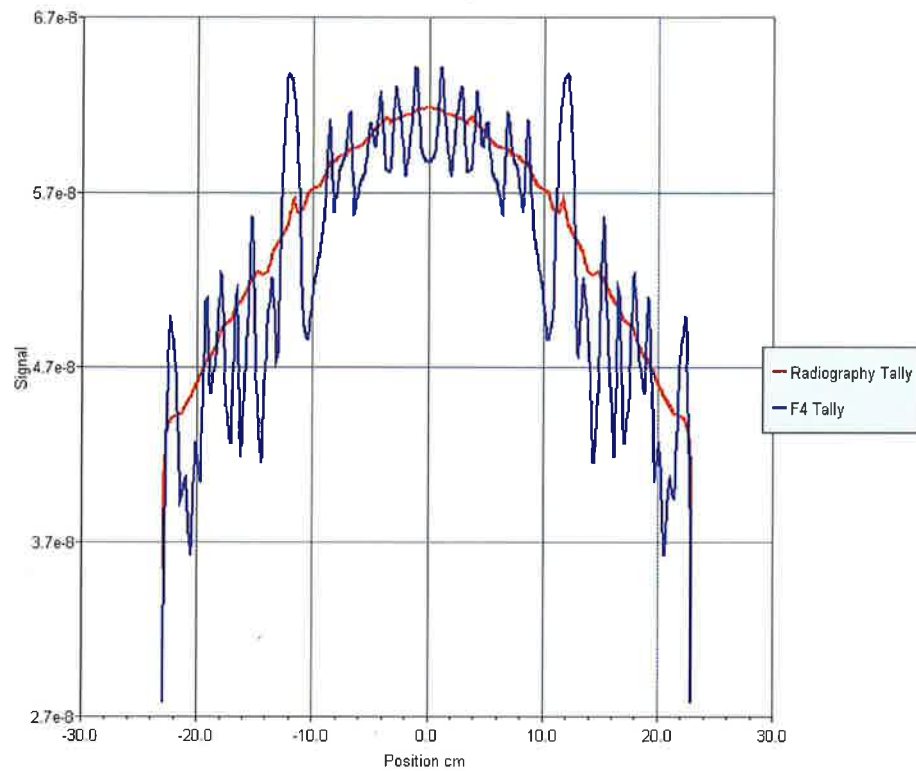


Figure 41 Comparison of Total Flat-Field Signals with 9.2 cm Tungsten in Bullnose

Examination of Figure 41 shows reasonable agreement between the two calculations. It is clear from Figure 41 that the F4 tally has too much noise despite running 7.7×10^{10} particles. Therefore, we utilize the radiographic simulation to perform a fit to the scatter simulation using an 8x8 order polynomial field. A comparison of the polynomial fit and the MCNP simulation using the radiographic tally for the total signal arising from the 9.2 cm of Tungsten in the bullnose in conjunction with the DARHT radiographic scene is presented in Figure 42.

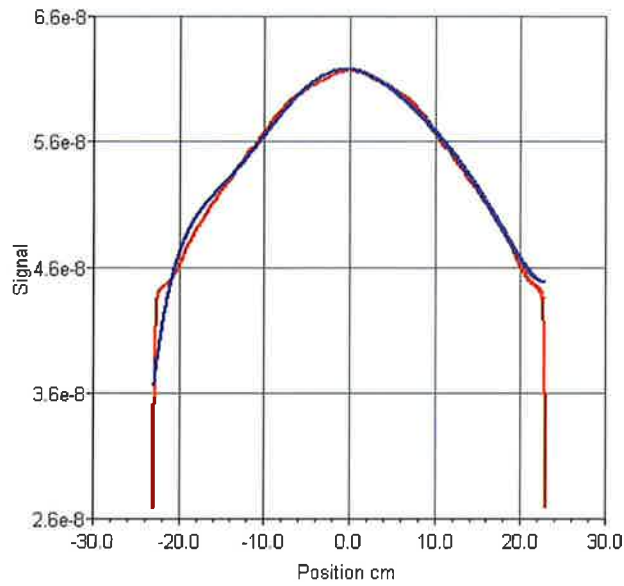


Figure 42 Comparison of the Polynomial Fit (8X8) to the Total Signal (Scatter plus direct)

Examination of Figure 42 illustrates the fact that the 8x8 polynomial fit of the radiographic tally simulation allows for an excellent comparison with the simulation.

Similarly, we utilize the radiographic tally to perform a functional fit of the scatter using an 8X8 polynomial. The results of this fit are presented in Figure 43.

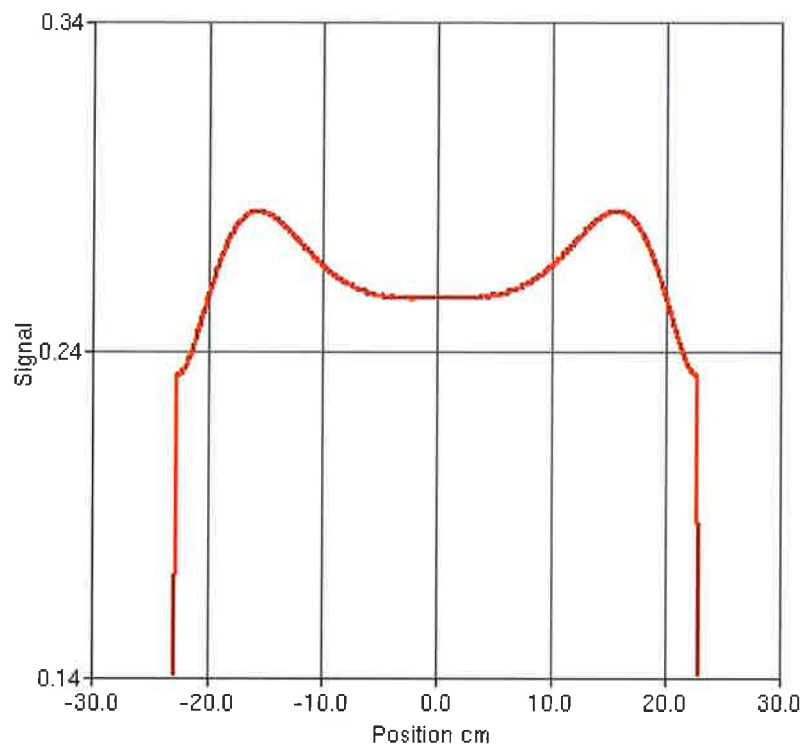


Figure 43 Ratio of Scatter to Direct 9.2 cm Tungsten

Examination of Figure 43 clearly demonstrates that the scatter is a significant fraction of the direct signal. Furthermore, the curvature in the ratio of the two fields clearly invalidates the previous assumption in which a constant was assumed across the image. This magnitude of scatter is in part attributed to the presence of the NDM as illustrated in Figure 44.

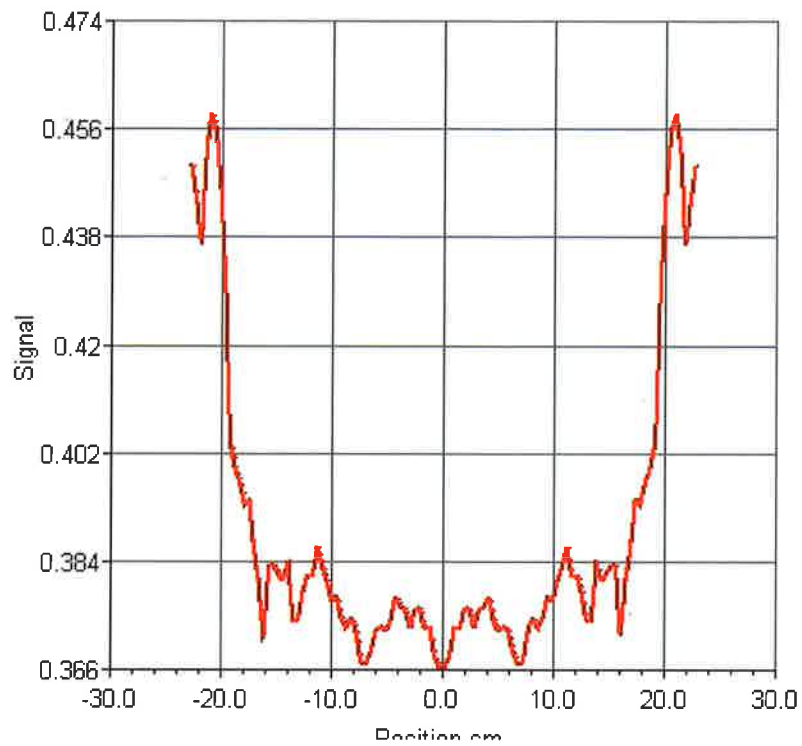


Figure 44 Ratio of Scatter 9.2 cm Tungsten in Bullnose w/o NDM / w NDM

Finally, the ratio of the direct to the total signal (direct plus scatter) is presented in Figure 45.

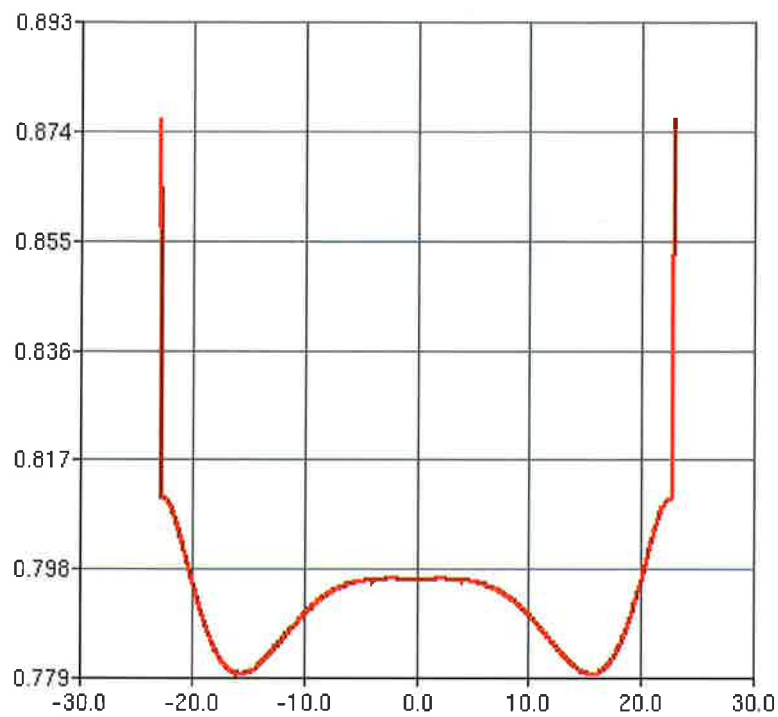


Figure 45 Ratio of Direct to Total 9.2 cm Tungsten in Bullnose

Examination of Figure 45 again reveals no constant behavior across the image.

4.1.5 FF Scatter with 11.2 cm of Tungsten in Bullnose

The results of the scatter field using the radiographic tally in which 11.2 cm of Tungsten was incorporated into the bullnose are presented in Figure 46.

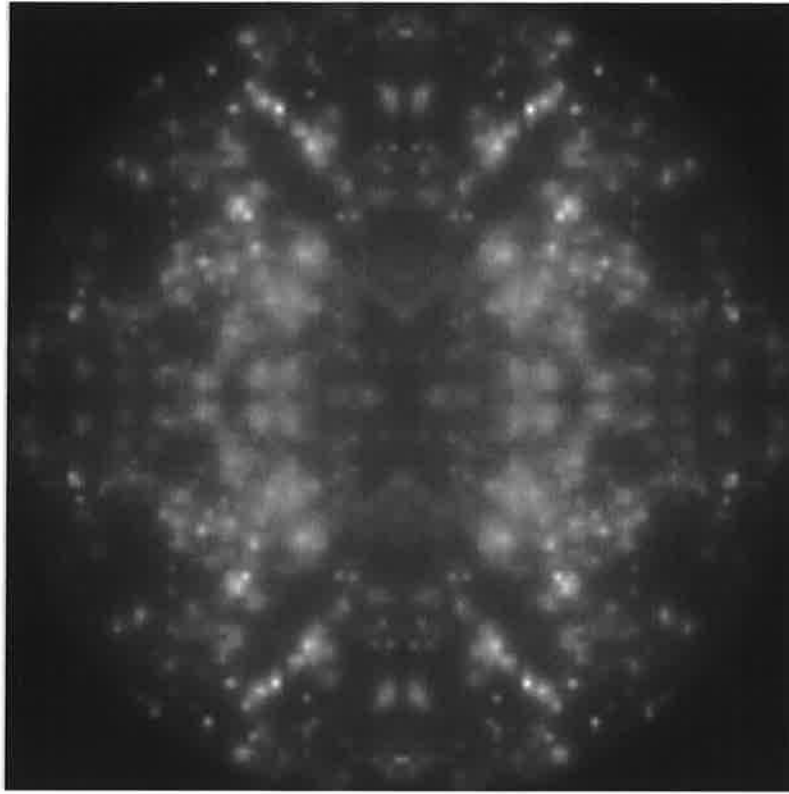


Figure 46 Scatter field from Radiographic Tally, 11.2 cm Tungsten in the Bullnose at the Image Plane

As may be observed, the results using the radiographic tally again have a significant number of flyers due to the proximity of the NDM to the image plane

A comparison of the polynomial fit and the MCNP simulation using the radiographic tally for the total signal arising from the 11.2 cm of Tungsten in the bullnose in conjunction with the DARHT radiographic scene is presented in Figure 47.

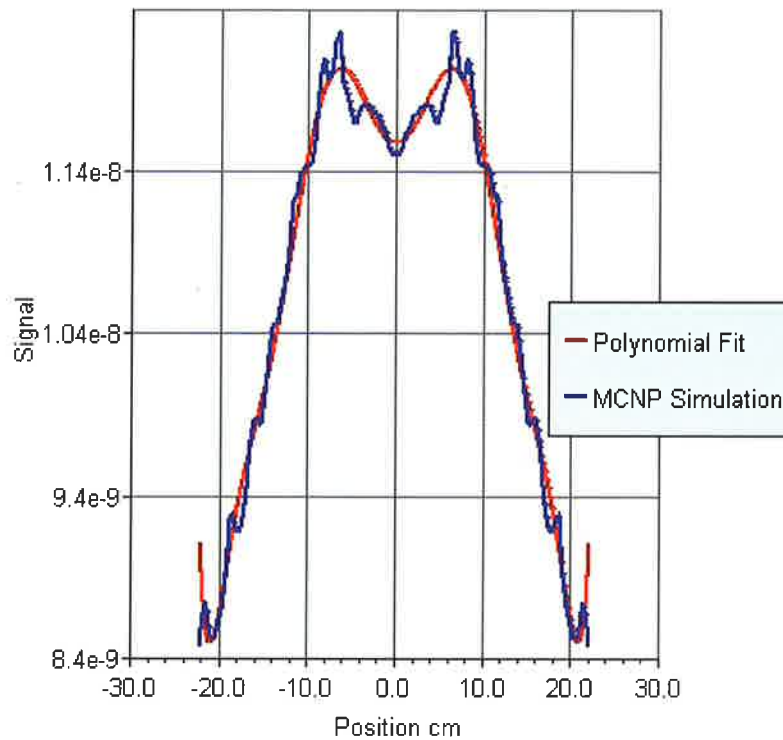


Figure 47 Comparison of the Polynomial Fit (12X12) to the Total Signal (Scatter plus direct) 11 cm Tungsten in Bullnose

Examination of Figure 47 illustrates the fact that the 12x12 polynomial fit of the radiographic tally simulation allows for an excellent comparison with the simulation. (It should be noted that additional degrees of freedom were needed to fit the 11.2 cm Tungsten case than the previous cases.)

Similarly, we utilize the radiographic tally to perform a functional fit of the scatter using a 12X12 polynomial. The results of this fit are presented in Figure 48.

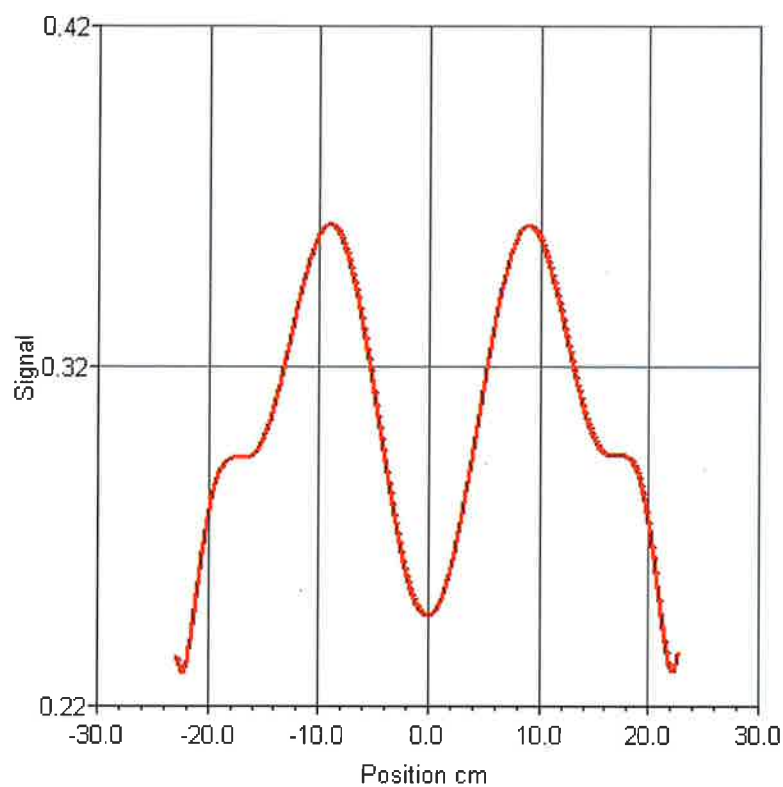


Figure 48 Ratio of Scatter to Direct 11 cm Tungsten

Examination of Figure 48 clearly demonstrates that the scatter is a significant fraction of the direct signal. Furthermore, the curvature in the ratio of the two fields clearly invalidates the previous assumption in which a constant was assumed across the image.

Finally, the ratio of the direct to the total signal (direct plus scatter) is presented in Figure 49.

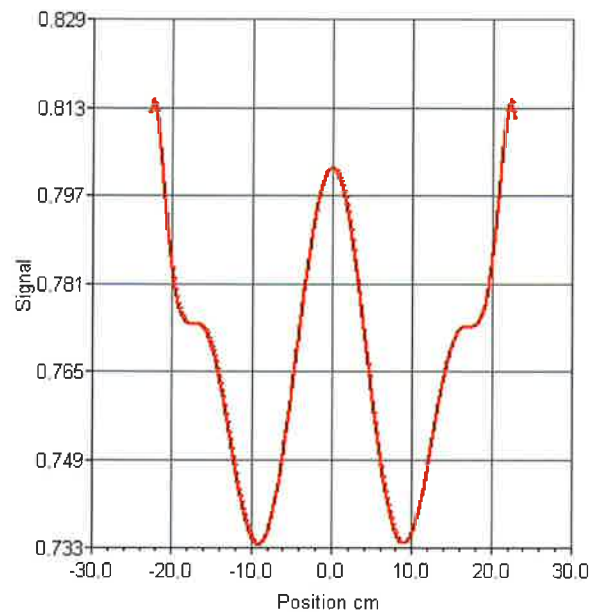


Figure 49 Ratio of Direct to Total 11.2 cm Tungsten in Bullnose

Examination of Figure 49 again reveals no constant behavior across the image.

5 Comparison of Simulation Flat-Field with Scatter and Experimental Data

To examine the ability of the transport simulation to match the experimental flat field a comparison of the experimental data with the flat-field obtained from the simulation was performed. For this comparison we utilized a scalar gain to calibrate the simulation to the data.

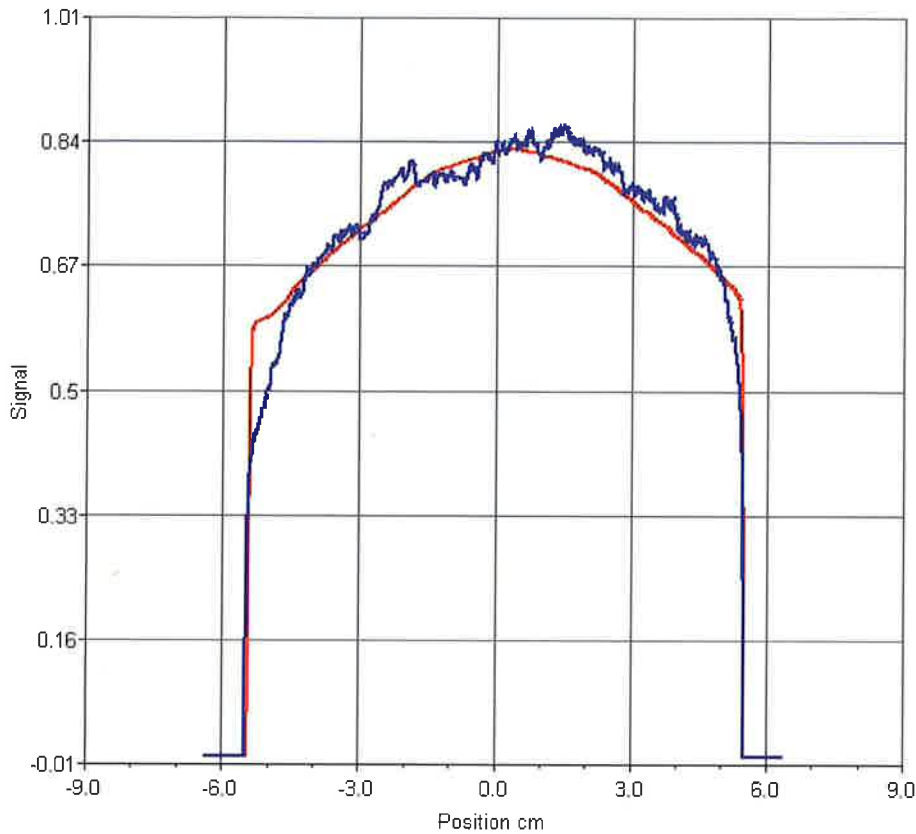


Figure 50 Comparison of the simulated flat-field 9.2 cm with the 3683 Axis 2 Time 1 Flat-Field 9.5 cm of Tungsten in the Bullnose

Examination of Figure 50 indicates a reasonable fit to the data. However, further investigation of the more rapid fall-off of the experimental signal is necessary. This more rapid fall-off of the experimental data may be attributed to lens effects. Furthermore, an investigation of an additional scatter attributed to the scene, i.e., ground surrounding buildings/objects/sky which is not easily incorporated into the simulation is also necessary. A series of experiments are being currently being planned to address these issue.

6 Proposed Forward Model/Ratio of Direct to Scatter and Functional fits

As we have shown above, a forward model that incorporates the scatter in the flat-field is required due to the significant scatter that may be present in the flat-field for typical DARHT radiographs. Using our formulation for the components of the forward model we have:

$$G''\left(\frac{\tilde{D}_{DFM}\tilde{B}_{PD}}{\tilde{B}_{PFF}+\tilde{S}_{FF}} + \frac{\tilde{S}_D}{\tilde{B}_{PFF}+\tilde{S}_{FF}}\right) \text{ Equation 11}$$

In implementing Equation 11 into the BIE forward model we allow the dynamic beam profile to shift and rotate relative to the beam profile of the flat-field.

7.0 Conclusions

An examination of the impact of scatter on the ratio of the scatter to direct signal was performed using MCNP6. Results indicate that the previous assumption that the scatter was insignificant is incorrect. Furthermore, as has been shown the ratio of scatter to direct or direct to the total signal exhibit non-constant behavior across the image with large deviations near the edge of the field of view. A modification to the forward model is proposed to incorporate this aspect of the physics model into all future BIE canvasses.

8.0 Acknowledgements

We would like to thank Jennifer Schei Disterhaupt and Sky Sjue for reading the manuscript and many useful discussions.

9.0 References

- ⁱ Physics Based Radiography, Klasky, M., LA-CP-18-00890, 2018
- ⁱⁱ DARHT Axis 2 Physics based Analysis and Uncertainties, LA-CP-18-00894, 2018
- ⁱⁱⁱ Overview of the Bayes Inference Engine (BIE): Fundamentals, Methodologies, Applications & Comparisons with Simulation, Tomkins, C. et. al., LA-CP 17-0084
- ^{iv} An experimental Study of Scatter Levels and Bucky Grid Performance at DARHT Using the FTO, Tomkins, C., Watson, S., Defense Research Journal Volume 17.1
- ^v Ibid ii
- ^{vi} Analysis of Hydro-Shot 3683/Final Forward Model, LA-CP-19-00189, 2019
- ^{vii} An examination of the Bucky Grid on Radiographic Performance at DARHT, Klasky, M., LA-CP-18-00819, 2108
- ^{viii} Ibid ii
- ^{ix} Ibid ii
- ^x Ibid ii